


Simulating higher-order topological insulators in density wave insulatorsKuan-Sen Lin and Barry Bradlyn ^{*}*Department of Physics and Institute for Condensed Matter Theory, University of Illinois at Urbana-Champaign, Urbana, Illinois 61801-3080, USA*

(Received 30 November 2020; accepted 20 April 2021; published 2 June 2021)

Since the discovery of the Harper-Hofstadter model, it has been known that condensed matter systems with periodic modulations can be promoted to nontrivial topological states with emergent gauge fields in higher dimensions. In this paper, we develop a general procedure to compute the gauge fields in higher dimensions associated to low-dimensional systems with periodic (charge- and spin-) density wave modulations. We construct two-dimensional (2D) models with modulations that can be promoted to higher-order topological phases with $U(1)$ and $SU(2)$ gauge fields in 3D. Corner modes in our 2D models can be pumped by adiabatic sliding of the phase of the modulation, yielding hinge modes in the promoted models. We also examine a 3D Weyl semimetal (WSM) gapped by charge-density wave (CDW) order, possessing quantum anomalous Hall surface states. We show that this 3D system is equivalent to a 4D nodal line system gapped by a $U(1)$ gauge field with a nonzero second Chern number. We explain the recently identified interpolation between inversion-symmetry protected phases of the 3D WSM gapped by CDWs using the corresponding 4D theory. Our results can extend the search for (higher-order) topological states in higher dimensions to density wave systems.

DOI: [10.1103/PhysRevB.103.245107](https://doi.org/10.1103/PhysRevB.103.245107)**I. INTRODUCTION**

Topological crystalline phases in noninteracting, clean structures have attracted a great deal of recent theoretical and experimental attention [1–6]. From the discovery of helical edge states in \mathbb{Z}_2 topological insulators (TIs) [7–9] to surface Dirac cones protected by time-reversal (TR) or crystal symmetries [2,10–12], the experimental manifestations of band topology have come primarily through the exploration of surface states. The recent theoretical prediction of higher-order topological insulators (HOTIs) [13–16] has triggered a wave of materials predictions [17–21] and experimental efforts to observe their predicted gapped surfaces but gapless corners (in 2D) or hinges (in 3D). At a theoretical level, topological band insulators can be classified by exploiting the constraints of symmetry, relating the topology of bands to the transformation properties of Bloch functions under crystal symmetries [14,17,22–29]. In the simplest cases, the symmetry eigenvalues of occupied electronic wave functions at different crystal momenta in the Brillouin zone can be used to deduce the absence of an exponentially localized, position space description of the occupied states, and hence the presence of nontrivial topology. Progress along these lines has led to a full, predictive classification of topological band structures both with and without time-reversal symmetry (TRS). Essential to these efforts is the presence of discrete translation symmetry, which ensures that localized electronic functions are identical in each unit cell, and hence allows the symmetry properties of the system to be described as a function of momentum.

At the same time, the interplay between topological bands and symmetry-breaking order has started to attract a great

deal of attention. It has been argued theoretically that in topological systems with charge-density wave (CDW) order, the collective phason mode of the CDW may inherit topological properties from the Fermi sea, such as an induced axion coupling to electromagnetic fields [30–34]. Signatures of this axion coupling have been recently experimentally detected in $(\text{TaSe}_4)_2\text{I}$ [35,36]. Additionally, the quantum anomalous Hall (QAH) phase in the Dirac semimetal ZrTe_5 can be understood as originating from a magnetic-field induced CDW transition [37–40]. Because CDW order is, in general, incommensurate with the underlying lattice, a full understanding of the interplay between mean-field CDW order and band topology requires us to examine topology of incommensurately modulated electronic systems. Such a study would also yield insights into topology in artificially modulated photonic [41,42], metamaterial [43], and cold-atomic lattice systems [44], which have become a focus of recent research due to their tunability and experimental accessibility.

Naively, the breaking of translational and point-group symmetries implied by incommensurate modulation would seem to prohibit the application of symmetry-based tools which have been so successful in identifying and classifying topological crystalline systems. However, it is often possible to view the single-particle dynamics in an incommensurately modulated system as describing the behavior of a particle in a larger number of dimensions, the phase offsets of the incommensurate modulations playing the role of momenta in the extra “synthetic” dimensions. The canonical example of this mapping is the 1D Harper (Aubry-André) model with incommensurate on-site potential. As was shown some time ago [45], the Hamiltonian for the Harper model is equivalent to the Hamiltonian for a 2D square-lattice system coupled to a background magnetic field [46,47]. The phase of the on-site modulation plays the role of the momentum in the second,

^{*}Corresponding author: bbradlyn@illinois.edu

synthetic dimension, while the wave vector of the modulation plays the role of the magnetic flux per plaquette in the 2D lattice. Bands in the enhanced, 2D system can be characterized by a Chern number, which mandates the presence of gapless chiral modes at the edges of the system. Reducing back to 1D, these 2D edge states manifest as boundary states of a 1D wire which appear and disappear as a function of the phase of modulation, thus realizing a Thouless pump [48–50]. Recent studies also show that certain generalization of the 1D Harper model allows for the investigation of higher-order topological phases [51].

In this paper, we will extend the connection beyond 1D to show how modulated systems in 2D and 3D can be related to topological crystalline phases in higher dimensions. We will first review a general method for representing a modulated system as a higher dimensional system coupled to a background gauge field [46–48,52]. For systems with negligible spin-orbit coupling and spin-independent modulation, the gauge field will be a U(1) magnetic field; for spin-dependent modulations, we will show that there can also be induced SU(2) gauge fields. We will exploit the fact that both U(1) and SU(2) gauge fields with constant field strength preserve inversion symmetry to show that 2D modulated systems can realize higher-order chiral [U(1)] and helical [SU(2)] topological phases in one extra synthetic dimension. We show how the hinge states of these synthetic HOTIs manifest as corner modes in 2D, with energies that can be tuned by changing the phase of the modulation. Going further, we use the mapping to synthetic dimensions to bring order to the complex landscape of eigenstates of the modulated system, showing how the states can be interpreted as bulk and surface Landau level (LL) wave functions in synthetic dimensions. Finally, we also revisit a 3D minimal model for a Weyl semimetal (WSM) with (generally incommensurate) CDW order [53], and show how it realizes a 4D nodal line semimetal gapped into a phase with a nontrivial second Chern number. We will verify our conclusions with a combination of exact numerical results and approximate low-energy analytic calculations. We will also exploit the fact that the phase of a (charge- or spin-) density wave (DW) order parameter can be shifted with an applied electromagnetic field by exciting the (nominally gapless but sometimes pinned) sliding mode [54]. This will allow us to make predictions about topological pumping of boundary states in modulated structures, driven by the sliding mode of the DW. In contrast to other recent proposals for topological pumping in synthetic dimensions, the coupling of the DW sliding mode to electromagnetic fields allows for tunability of synthetic dimensions in modulated structures. We will comment on potential experimental realizations in condensed matter, photonic, and cold-atom systems throughout. This paper will enable avenues for exploring higher-order topological phenomena which, with the exception of some promising results in bismuth [55–57], have not been unambiguously identified in crystalline electronic systems.

The rest of the paper is organized as follows. In Sec. II, we review how the Thouless pump in a 1D Rice-Mele [Su-Schrieffer-Heeger (SSH)] chain is realized by the sliding of a CDW, and we review its connection to topology by promoting the model to a 2D π -flux lattice. In Sec. III, we next develop a general method to compute the U(1) gauge fields that are

coupled to a higher dimensional models promoted from a low-dimensional modulated system. In Secs. IV and V, we construct 2D modulated systems that can be promoted to 3D chiral and helical HOTIs coupled to U(1) and SU(2) gauge fields, respectively. We demonstrate the pumping of corner modes by the sliding of DWs in these systems via numerical calculations of the energy spectra. We examine the properties of wave functions in these 2D modulated systems by constructing low-energy theories coupled to gauge fields in 3D. We show how the evolution of bulk, edge, and corner states in 2D can be understood from the perspective of the low-energy theory in 3D. In Sec. VI, we turn to a model for a 3D WSM gapped by a CDW. We show that this model can be promoted to a 4D nodal line system gapped by a U(1) gauge field. We derive the corresponding low-energy theory in 4D and use it to explain both the existence of QAH surface states and the interpolation between topologically distinct QAH phases at the two inversion-symmetric values of the CDW phase in this 3D system. Finally, in Sec. VII, we give an outlook as to how our work may extend the search of (higher-order) TIs in higher dimensions and enable simulations of SU(2) gauge physics in higher dimensions. Some details of our models, further numerical results, and detailed derivations of the low-energy theories are presented in the Supplemental Material (SM) [58].

Throughout this paper, we use units where $\hbar = c = |e| = 1$, and where the electron has charge $-|e| = -1$. Furthermore, the Einstein summation convention will not be used; whenever there is a summation over an index, we will write the summation explicitly.

II. REVIEW: THOULESS PUMP AS SLIDING MODE

In this section, we review the CDW picture of the Rice-Mele (SSH) model [52,59], and the interpretation of the Thouless pump [48] as a CDW sliding mode. Consider the following Hamiltonian for a 1D chain:

$$H_{\text{Rice-Mele}} = \sum_n (t + \delta t (-1)^n \cos \phi) c_{n+1}^\dagger c_n + \text{H.c.} + \sum_n (-1)^{n+1} \Delta \sin \phi c_n^\dagger c_n, \quad (1)$$

where c_n^\dagger is the creation operator for an electron at site n . The nearest-neighbor hopping and on-site potential are modulated with periodicity 2 and their relative strength is related to the phase ϕ of the modulation. We thus identify ϕ as the phase of this CDW modulation. In this paper, we use the terms CDW sliding phase and phases of the mean-field CDW order parameter interchangeably to refer to ϕ . For suitable choices of t , δt , and Δ , the spectrum of this Hamiltonian is gapped for all $\phi \in [0, 2\pi)$. Focusing on the half-filled insulating ground state in this parameter regime, the occupied-band Wannier centers [17,60–63] will be pumped by a length of one unit cell (two sites) as the phase ϕ adiabatically slides from 0 to 2π , leading to a quantized change of bulk polarization [52,64–66]. This quantization has a topological origin: If we regard ϕ as a crystal momentum along a second, synthetic dimension which we call y , Eq. (1) is equivalent to a 2D square lattice model with a U(1) π -flux (equivalent to half

flux quantum $\Phi_0 = 2\pi\hbar/|e|$ where electron has charge $-|e|$ per plaquette, and with a fixed crystal momentum k_y along y . The quantized polarization change is then identified as the Chern number [49,65,67–69] of the occupied bands in 2D. We provide further details, including numerical verification of charge pumping, and the explicit construction of the dimensional promotion to 2D, in the SM [58].

We see from this example that promoting the dimension of a modulated system to a higher dimensional lattice coupled to gauge fields can help explain the topological origin of low-dimensional properties, including charge transport and boundary modes. A general method for dimensional promotion will thus be helpful in dealing with various topological modulated systems in more than 1D. In what follows, we will show that the dimensional promotion approach can be extended to higher dimensions and to cases where the modulation is incommensurate with the underlying lattice periodicity.

III. DIMENSIONAL PROMOTION PROCEDURE

In this section, we will generalize the 1D-to-2D promotion of the Rice-Mele chain to general dimensions. To begin, let us consider a d -dimensional (d D) electronic model on a cubic lattice with N mutually incommensurate on-site modulations [46,47,70–73] described by the Hamiltonian

$$H_{\text{low-dim}} = \sum_{\vec{n}, \vec{m}} \psi_{\vec{n}+\vec{m}}^\dagger [H_{\vec{m}}] \psi_{\vec{n}} + \sum_{\vec{n}} \sum_{i=1}^N \psi_{\vec{n}}^\dagger [V_{\vec{n}}^{(i)}] \psi_{\vec{n}}. \quad (2)$$

Here both $\vec{n} = (n_1, \dots, n_d)$ and $\vec{m} = (m_1, \dots, m_d) \in \mathbb{Z}^d$ are vectors in the d D cubic lattice, and $\psi_{\vec{n}}^\dagger$ is the electron creation operator for an electron at position \vec{n} with a given set of spin and orbital degrees of freedom. We denote by $[H_{\vec{m}}]$ the hopping matrix connecting position \vec{n} to $\vec{n} + \vec{m}$, and by $[V_{\vec{n}}^{(i)}]$ the matrix representing i th modulated on-site energy at position \vec{n} ($i = 1, \dots, N$), with matrix indices encoding the spin and orbital dependence of the hopping [74]. Note that Hermiticity of the Hamiltonian requires that $[H_{\vec{m}}] = [H_{-\vec{m}}]^\dagger$ and $[V_{\vec{n}}^{(i)}]^\dagger = [V_{\vec{n}}^{(i)}]$. We further assume that $[V_{\vec{n}}^{(i)}] = [f^{(i)}(2\pi\vec{q}^{(i)} \cdot \vec{n} + \phi^{(i)})]$ with $[f^{(i)}(x)] = [f^{(i)}(x + 2\pi)]$, where $\vec{q}^{(i)}$ is the i th modulation wave vector and $\phi^{(i)}$ is the sliding phase associated with the i th modulation. For the cubic system with unit lattice vectors we are discussing here, each component $q_j^{(i)}$ ($j = 1, \dots, d$) of $\vec{q}^{(i)}$ is defined within $[0,1)$; that is, each $2\pi\vec{q}^{(i)}$ lies within the primitive Brillouin zone of the unmodulated system. Since each $[V_{\vec{n}}^{(i)}]$ is a periodic function, they can be expanded in terms of Fourier series as

$$[V_{\vec{n}}^{(i)}] = \sum_{p_i \in \mathbb{Z}} [V_{p_i}^{(i)}] e^{ip_i(2\pi\vec{q}^{(i)} \cdot \vec{n} + \phi^{(i)})}, \quad (3)$$

where $[V_{p_i}^{(i)}]$ is the matrix-valued p_i th Fourier component of $[V_{\vec{n}}^{(i)}]$. Note that $[V_{p_i}^{(i)}] = [V_{-p_i}^{(i)}]^\dagger$ due to Hermiticity of the Hamiltonian.

To perform the enhancement of dimensions, we first insert the expansion Eq. (3) into the Hamiltonian Eq. (2). We then regard each $\phi^{(i)}$ as the i th crystal momentum k^i along one of the additional N synthetic dimensions. We then promote the d D model to a $(d+N)$ D space by summing over $\vec{k} =$

$(k^1, \dots, k^N) \in \mathbb{T}^N$ (where \mathbb{T}^N denotes the N -dimensional torus), which yields the Hamiltonian in $(d+N)$ D as

$$H_{\text{high-dim}} = \sum_{\vec{n}, \vec{m}, \vec{k}} \psi_{\vec{n}+\vec{m}, \vec{k}}^\dagger [H_{\vec{m}}] \psi_{\vec{n}, \vec{k}} + \sum_{\vec{n}, \vec{k}, i, p_i} \psi_{\vec{n}, \vec{k}}^\dagger [V_{p_i}^{(i)}] e^{ip_i k^i} e^{i2\pi p_i \vec{q}^{(i)} \cdot \vec{n}} \psi_{\vec{n}, \vec{k}}. \quad (4)$$

Each physically distinct configuration of $\{\phi^{(i)}\}$ can be recovered by restricting the Hamiltonian Eq. (4) to a single \vec{k} point. Once we sum over \vec{k} , however, we can reinterpret the Hamiltonian in a $(d+N)$ D space. As we will see below, adiabatic pumping of the phases $\phi^{(i)}$ by an external field will allow us to explore dynamics in the full $d+N$ dimensional space.

To obtain the $(d+N)$ D model in position space, we perform an inverse Fourier transform of $\psi_{\vec{n}, \vec{k}}^\dagger$, yielding

$$H_{\text{high-dim}} = \sum_{\vec{n}, \vec{m}, \vec{v}} \psi_{\vec{n}+\vec{m}, \vec{v}}^\dagger [H_{\vec{m}}] \psi_{\vec{n}, \vec{v}} + \sum_{\vec{n}, \vec{v}, i, p_i} \psi_{\vec{n}, \vec{v}-p_i \hat{v}_i}^\dagger [V_{p_i}^{(i)}] e^{i2\pi p_i \vec{q}^{(i)} \cdot \vec{n}} \psi_{\vec{n}, \vec{v}}, \quad (5)$$

where $\vec{v} = (v_1, \dots, v_N) \in \mathbb{Z}^N$ and \hat{v}_i is the unit vector along the i th additional dimension, such that $\vec{v} - p_i \hat{v}_i = (v_1, \dots, v_i - p_i, \dots, v_N)$. Equation (5) can be viewed as the Hamiltonian for a system on a $(d+N)$ D cubic lattice whose lattice sites are located at $(\vec{n}, \vec{v}) = (n_1, \dots, n_d, v_1, \dots, v_N) \in \mathbb{Z}^{d+N}$. The system is coupled to a continuous $U(1)$ gauge field

$$\vec{A} = \left(\underbrace{\vec{0}}_{dD}, \underbrace{2\pi\vec{q}^{(1)} \cdot \vec{r}, \dots, 2\pi\vec{q}^{(N)} \cdot \vec{r}}_{ND} \right) \quad (6)$$

through a Peierls substitution [75], explaining the appearance of the phase factors multiplying $[V_{p_i}^{(i)}]$ in Eq. (5). Note $\vec{r} \in \mathbb{R}^d$ is a vector in the original d D space.

As the vector potential in Eq. (6) is linear in position \vec{r} , the antisymmetric field strength $F_{\mu\nu} = \partial_\mu A_\nu - \partial_\nu A_\mu$ is constant in space. In particular, Eq. (6) implies that the nonzero components of $F_{\mu\nu}$ are given by

$$F_{i, j+d} = \partial_i A_{j+d} - \partial_{j+d} A_i = \partial_i A_{j+d} = 2\pi q_i^{(j)}, \quad (7)$$

where $i = 1, \dots, d$ and $j = 1, \dots, N$. Due to the antisymmetry of the field strength, $F_{i+d, j}$ with $i = 1, \dots, N$, $j = 1, \dots, d$ is also nonzero and given by $F_{i+d, j} = -2\pi q_j^{(i)}$. Therefore, the (nonzero) constant field strength is proportional to the magnitude of the modulation wave vectors.

This shows that a d D modulated system with phase offset $\{\phi^{(i)}\}$ is equivalent to the Bloch Hamiltonian [see Eq. (4)] of the promoted $(d+N)$ D lattice model with fixed crystal momenta \vec{k} , once we identify $\phi^{(i)}$ as k^i . In practice, the modulation $[V_{\vec{n}}^{(i)}]$ can be induced by a set of DW modulations. The phase offset $\{\phi^{(i)}\}$ is then regarded as the phason degrees of freedom, namely, the phase of the i th mean-field DW order parameter. By applying electric fields that depin the DWs and make them slide [35,54,76], we may sample the whole spectrum of the $(d+N)$ D model. In particular, and as we will explore in subsequent sections, nontrivial topology in the $(d+N)$ D lattice model—which may support localized boundary states—will manifest in the response of the d D

model to adiabatic sliding of the DW phase mode(s). We emphasize here that in our dimensional promotion procedure for a DW system, there are no emergent electric fields in the promoted $(d + N)$ D space. The electric fields mentioned here are external and serve as a way to depin the DW to vary $\{\phi^{(i)}\}$ adiabatically. This allows for the sampling of the entire spectrum of the $(d + N)$ D model as a function of $\{\phi^{(i)}\}$, namely, the additional crystal momenta.

Before we move on to consider the band topology of promoted lattice models, let us make a few general comments about our dimensional promotion procedure. First, note that the dimensional promotion procedure places no constraints on the modulation vectors $\vec{q}^{(i)}$; in particular, they need not be commensurate with the underlying lattice. In the case of incommensurate modulation, the dimensional promotion procedure allows us to write the d D incommensurate model in terms of a periodic $(d + N)$ D model with an irrational U(1) flux per plaquette. We will see below how we can use this to explore the topology of systems with incommensurate modulation. We emphasize that the dimensional promotion procedure is independent of whether in the original d D space the system is infinite or finite. When we promote the dimension of a d D system to $(d + N)$ D space, the $(d + N)$ D system is inherently infinite along the additional N dimensions, as it allows a Fourier transformation to obtain the Bloch Hamiltonian with fixed N additional crystal momenta. From this viewpoint, there are two ways to utilize the dimensional promotion procedure. If we promote the dimension of an infinite d D system, we will obtain an infinite $(d + N)$ D system that allows us to discuss the nontrivial bulk topology in the promoted $(d + N)$ D space. If we instead promote the dimension of a finite d D system, we will obtain a $(d + N)$ D system which is finite along the original d dimensions and infinite in the additional N dimensions. This allows us to compute the energy spectrum to examine whether there are boundary states protected by the nontrivial bulk topology in $(d + N)$ D space.

Second, although here we consider only dimensional promotion of a d D cubic lattice model with only on-site modulations and all orbitals located at the lattice points labeled by $\vec{n} \in \mathbb{Z}^d$ to a $(d + N)$ D cubic lattice model, we may generalize our method to d D models with modulations in both on-site and hopping matrix elements, together with nonorthogonal lattice vectors and arbitrary orbital positions. We show how to systematically promote the dimensions of such d D models to $(d + N)$ D and compute the corresponding U(1) gauge fields in the SM [58]. We also give several examples in the SM [58], including the dimensional promotion of (1) the 1D Rice-Mele chain in Sec. II to a 2D square lattice with π flux, (2) 1D lattices with modulation in both on-site energies and hopping terms to 2D hexagonal lattices under a perpendicular magnetic field, and (3) 2D modulated systems with hexagonal lattice to 3D systems also with hexagonal lattices coupled to a U(1) gauge field. The U(1) gauge fields will take a slightly different form from Eq. (6) when we consider a system with nonorthogonal lattice vectors. However, the vector potentials will still be linear in $\vec{r} \in \mathbb{R}^{d+N}$, and hence will still produce constant field strengths $F_{\mu\nu}$. Furthermore, note that although we considered for simplicity models where the electrons were localized to the origin of each unit cell, this is not essential for the application of our formalism.

Third, we emphasize that no additional parameters are used in the above derivation. The hopping matrices connecting (\vec{n}, \vec{v}) to $(\vec{n} + \vec{m}, \vec{v})$ and $(\vec{n}, \vec{v} - p_i \hat{v}_i)$ are given by $[H_{\vec{m}}]$ and $[V_{p_i}^{(i)}]$, respectively, in the $(d + N)$ D model. The phase $\phi^{(i)}$ corresponds to the i th crystal momentum along the i th additional dimensions. Further, the modulation wave vectors $\vec{q}^{(i)}$ specify the strength of the U(1) gauge field in $(d + N)$ D, see Eq. (6). Notice that the on-site modulations $[V_{\vec{n}}^{(i)}]$ only lead to hopping parallel to \hat{v}_i in $(d + N)$ D. If we also consider modulated hopping matrices in d D, upon dimensional promotion we will get hopping along $\vec{m} + p_i \hat{v}_i$ in $(d + N)$ D [46,77], which we show in the SM [58]. Notice that the index i is not summed over in $p_i \hat{v}_i$. Recall also that \vec{m} and \hat{v}_i are vectors in the original d D and additional N D space, respectively. An example that demonstrates this is the 1D Rice-Mele model [52] in Sec. II. In the SM [58], we promote Eq. (1) to a 2D lattice with π flux per plaquette in which the electrons can hop along $\hat{x} + \hat{y}$ (where \hat{x} and \hat{y} are in the original 1D and additional 1D space, respectively).

Next, our construction provides a way to compute the promoted $(d + N)$ D model and the U(1) gauge field to which it is coupled. As a U(1) gauge field breaks TRS, this dimensional promotion procedure is suitable to investigate nontrivial topological phases in $(d + N)$ D space without TRS. Below we will also consider a dimensional promotion to $(d + N)$ D space with an SU(2) gauge field, which preserves TRS and allows us to explore nontrivial topological phases protected by TRS [7,8,78,79]. To construct a low-dimensional modulated model equivalent to a higher dimensional lattice coupled to an SU(2) gauge field, we adopt a top-down approach. We will in Sec. V present a 2D modulated model which is obtained from a 3D model coupled to one SU(2) gauge field with a fixed crystal momentum.

In the following sections, we explore various 2D and 3D modulated systems that admit a dimensional promotion to a higher dimensional topological phases coupled to either U(1) or SU(2) gauge fields. We will show how an analysis of the higher-dimensional models can shed light on the eigenstates and boundary state dynamics of incommensurate DWs.

IV. CHIRAL HIGHER-ORDER TOPOLOGICAL SLIDING MODES

In this section, we will show how the dimensional promotion procedure can be used to realize 3D chiral HOTIs in 2D DW materials. We will first construct a Hamiltonian for an insulating 2D modulated system that is inversion symmetric for special values of the DW sliding phase ϕ . Then, we will show how, after dimensional promotion, the Hamiltonian corresponds to a 3D inversion-symmetric chiral HOTI coupled to a U(1) gauge field. We will explore the connection between hinge states of the 3D system and corner states of the 2D system using a combination of numerical diagonalization and a 3D low-energy $\vec{k} \cdot \vec{p}$ theory.

A. Dimensionally promoted chiral model

Consider the following 2D Hamiltonian for electrons on a square lattice, with one modulated on-site potential

$[V(\vec{q}, \vec{n}, \phi)]:$

$$H = \sum_{\vec{n}} \psi_{\vec{n}+\hat{x}}^\dagger [H_{+\hat{x}}] \psi_{\vec{n}} + \psi_{\vec{n}+\hat{y}}^\dagger [H_{+\hat{y}}] \psi_{\vec{n}} + \text{H.c.} \\ + \sum_{\vec{n}} \psi_{\vec{n}}^\dagger ([H_{\text{on-site}}] + [V(\vec{q}, \vec{n}, \phi)]) \psi_{\vec{n}}, \quad (8)$$

where the unmodulated hoppings and on-site energies are

$$[H_{+\hat{i}}] = \frac{J_i}{2} \tau_z \sigma_0 - \frac{\lambda_i}{2i} \tau_x \sigma_i, \quad (9)$$

$$[H_{\text{on-site}}] = M \tau_z \sigma_0 + \tau_0 \vec{B}_0 \cdot \vec{\sigma}. \quad (10)$$

We use \hat{e}_i to denote the unit vector along the i th ($i = 1, 2$) direction. The Pauli matrices $\vec{\tau} = (\tau_x, \tau_y, \tau_z)$ and $\vec{\sigma} = (\sigma_x, \sigma_y, \sigma_z)$ denote, respectively, orbital (for example, s and p orbitals) and spin degrees of freedom. This Hamiltonian is inversion symmetric, with inversion symmetry represented by τ_z . Furthermore, when $\vec{B}_0 = 0$, the model is also TR symmetric, with the TR operator represented as $i\sigma_y \mathcal{K}$ (where \mathcal{K} is the complex conjugation operator).

We assume that both orbital degrees of freedom are located at the lattice sites. The hopping matrices $[H_{+\hat{i}}]$, and $M \tau_z \sigma_0$ give rise to, at low energy, four-component massive Dirac fermions, allowing us to access various topological phases [69,78,80]. Physically, we can interpret $M \tau_z \sigma_0$ as the on-site energy difference for different orbitals and $\tau_0 \vec{B}_0 \cdot \vec{\sigma}$ as a ferromagnetic potential which splits the spin degeneracy of bands [81]. The modulated on-site potential, which can arise from a DW modulation, is

$$[V(\vec{q}, \vec{n}, \phi)] = J_z \cos \theta_{\vec{q}, \vec{n}, \phi} \tau_z \sigma_0 + \lambda_z \sin \theta_{\vec{q}, \vec{n}, \phi} \tau_x \sigma_z, \quad (11)$$

where $\theta_{\vec{q}, \vec{n}, \phi} = 2\pi \vec{q} \cdot \vec{n} + \phi$, $\vec{q} = (q_x, q_y)$ is the modulation wave vector in 2D, $\vec{n} \in \mathbb{Z}^2$ is the lattice position, and ϕ is

the sliding phase. The first term in Eq. (11) modulates the mass $M \tau_z \sigma_0$ in Eq. (10), while the second modulation denotes an on-site spin-orbit coupling between s and p orbitals. Note that the modulation $J_z \cos \theta_{\vec{q}, \vec{n}, \phi} \tau_z \sigma_0$ is a TR-even charge ordering, while $\lambda_z \sin \theta_{\vec{q}, \vec{n}, \phi} \tau_x \sigma_z$ is a TR-odd spin ordering. To see this, note that TR maps $(\tau_0, \tau_x, \tau_y, \tau_z) \rightarrow (\tau_0, \tau_x, -\tau_y, \tau_z)$ and $(\sigma_0, \sigma_x, \sigma_y, \sigma_z) \rightarrow (\sigma_0, -\sigma_x, -\sigma_y, -\sigma_z)$. In addition, the modulations $J_z \cos \theta_{\vec{q}, \vec{n}, \phi} \tau_z \sigma_0$ and $\lambda_z \sin \theta_{\vec{q}, \vec{n}, \phi} \tau_x \sigma_z$ are both inversion symmetric when $\phi = 0, \pi$.

Denoting the third, synthetic dimension as z and identifying ϕ as the corresponding crystal momentum k_z , we may use our general procedure in Sec. III to promote this 2D modulated system to a 3D lattice model. We first expand the modulations in terms of Fourier series as

$$J_z \cos \theta_{\vec{q}, \vec{n}, \phi} \tau_z \sigma_0 = \frac{J_z}{2} (e^{i\theta_{\vec{q}, \vec{n}, \phi}} + e^{-i\theta_{\vec{q}, \vec{n}, \phi}}) \tau_z \sigma_0, \quad (12)$$

$$\lambda_z \sin \theta_{\vec{q}, \vec{n}, \phi} \tau_x \sigma_z = \frac{\lambda_z}{2i} (e^{i\theta_{\vec{q}, \vec{n}, \phi}} - e^{-i\theta_{\vec{q}, \vec{n}, \phi}}) \tau_x \sigma_z. \quad (13)$$

According to Eqs. (3) and (5), the hopping along $+\hat{z}$ can be identified with the terms associated with $e^{-i\theta_{\vec{q}, \vec{n}, \phi}}$ in Eqs. (12) and (13). Therefore, the hopping along $+\hat{z}$ in the promoted 3D space reads

$$[H_{+\hat{z}}] = \frac{J_z}{2} \tau_z \sigma_0 - \frac{\lambda_z}{2i} \tau_x \sigma_z. \quad (14)$$

From Eq. (6), we can also identify the vector potential in the promoted 3D space as

$$\vec{A} = (0, 0, 2\pi \vec{q} \cdot \vec{r}) = (0, 0, 2\pi q_x x + 2\pi q_y y), \quad (15)$$

where $\vec{r} = (x, y) \in \mathbb{R}^2$. Therefore, we have that the lattice Hamiltonian in the promoted 3D space is given by

$$H = \sum_{\vec{n}} [(\psi_{\vec{n}+\hat{x}}^\dagger [H_{+\hat{x}}] \psi_{\vec{n}} + \psi_{\vec{n}+\hat{y}}^\dagger [H_{+\hat{y}}] \psi_{\vec{n}} + \psi_{\vec{n}+\hat{z}}^\dagger [H_{+\hat{z}}] e^{-i2\pi(q_x n_x + q_y n_y)} \psi_{\vec{n}} + \text{H.c.}) + \psi_{\vec{n}}^\dagger [H_{\text{on-site}}] \psi_{\vec{n}}], \quad (16)$$

where the vector potential Eq. (6) is coupled to the system through a Peierls substitution [75], and $[H_{+\hat{x}}]$, $[H_{+\hat{y}}]$, $[H_{+\hat{z}}]$ and $[H_{\text{on-site}}]$ are given by Eqs. (9) and (10), respectively. Hereafter, we will set $J_x = J_y = J_z = J$ for simplicity. If we Fourier transform Eq. (16) along z and regard k_z (the wave number along z) as the sliding phase ϕ , we can obtain the 2D modulated system in Eq. (8).

We will now use Eq. (16) to analyze the topological properties of the higher-dimensional model to infer the properties of the low-dimensional modulated system. This approach can also be employed in other low-dimensional modulated systems provided the corresponding higher-dimensional models are constructed. For $q_x = q_y = 0$ and $\vec{B}_0 = 0$, Eq. (16) describes a TR and inversion-symmetric insulator whose inversion operation is represented by τ_z (note that inversion symmetry acts to flip the sign on the synthetic momentum k_z). We can employ the theory of symmetry-based indicators of band topology [14,21,22,26,53,82–84] to compute the \mathbb{Z}_4

indicator,

$$z_4 = \frac{1}{4} \sum_{\vec{k}_a \in \text{TRIMs}} (n_+^a - n_-^a) \bmod 4, \quad (17)$$

where $n_+^a [n_-^a]$ is the number of positive[negative] parity eigenvalues in the valence band at the time-reversal invariant momentum (TRIM) \vec{k}_a . We find that for $|M/J| > 3$, $|M/J| < 1$, $1 < M/J < 3$, $-3 < M/J < -1$, the \mathbb{Z}_4 symmetry-based indicator is given by $z_4 = 0, 0, 1$ and 3 , respectively. The regimes where $z_4 \bmod 2 = 1$ give a strong TRS-invariant TI. For nonzero \vec{B}_0 which breaks TRS but does not induce additional band inversions, the magnetic \mathbb{Z}_4 symmetry-based indicator [14,15,17,21,26–29,53,81,85–87] is given by

$$\tilde{z}_4 = \frac{1}{2} \sum_{\vec{k}_a \in \text{TRIMs}} (n_+^a - n_-^a) \bmod 4, \quad (18)$$

such that for $|M/J| > 3$, $|M/J| < 1$, $1 < |M/J| < 3$ we have $\tilde{z}_4 = 0, 0$, and 2 . The corresponding weak indices are all

necessarily trivial. Therefore, for $1 < |M/J| < 3$ with $q_x = q_y = 0$, the system described by Eq. (16) gives a strong TI with $\vec{B}_0 = 0$ and a chiral HOTI (axion insulator) [26] with $\vec{B}_0 \neq 0$, where the gapless surface states of the strong TI are gapped by the inversion-preserving ferromagnetic potential $\tau_0 \vec{B}_0 \cdot \vec{\sigma}$. Therefore, Eq. (16) with $\vec{q} \neq 0$ describes an inversion-symmetric chiral HOTI [88] coupled via a Peierls substitution to a 3D U(1) gauge field given by the \vec{A} in Eq. (6). This \vec{A} produces a constant U(1) magnetic field,

$$\nabla \times \vec{A} = (2\pi q_y, -2\pi q_x, 0), \quad (19)$$

which preserves the inversion symmetry represented by τ_z in 3D, up to a gauge transformation (see SM [58]). Therefore, for a suitable choice of parameters, as long as the U(1) gauge field does not close the bulk gap in 3D, the insulating ground state will be in the same inversion symmetry-protected nontrivial chiral HOTI phase. This implies that our model should exhibit the characteristic boundary modes of a chiral HOTI in 3D. In particular, our promoted model will support odd numbers of sample-encircling chiral hinge modes in rod geometries which respect inversion symmetry [53,81,88].

B. Corner states

Recalling that in our case the \hat{z} direction is conjugate to the phase ϕ of the sliding mode (regarded as the crystal momentum k_z), it is natural for us to consider inversion-symmetric rod geometries which are finite in the \hat{x} and \hat{y} directions and infinite in the \hat{z} direction. In our 2D system, this corresponds to considering the properties of a finite system as a function of the phase ϕ . We can thus compute the energy spectrum of our 2D system in an open geometry with size $L_x \times L_y$ as a function of ϕ to obtain the energy dispersion along k_z in the promoted model. In the following, we call this kind of calculation the *ϕ -sliding spectrum*, since the variation of ϕ can be obtained by electromagnetically exciting the sliding mode of the underlying DW. Figure 1(a) shows the ϕ -sliding spectrum of Eq. (8) with parameters $J = 1$, $M = 2$, $\lambda_i = 1$, $(\vec{B}_0)_i = 0.5/\sqrt{3}$ [88], and $\vec{q} = (0, q_y)$, where $q_y = 0.11957$ is comparable with the experimental CDW wave vectors in $(\text{TaSe}_4)_2\text{I}$ [36] and is incommensurate with the underlying 2D square lattice in Eq. (8). The system size is 31×31 . As we can see, the spectrum contains modes which, as a function of ϕ , traverse the bulk spectral gap. Examining the wave functions of these gap-crossing modes, we see that they are localized to the corners of our 2D sample, as shown in Fig. 1(b). The gap-crossing modes with opposite slopes correspond to states at inversion-related corners; in our example, one mode is localized at the corner $(x_{\text{corner}}, y_{\text{corner}}) = (L/2, -L/2)$ [Fig. 1(b)] and the other at $(x_{\text{corner}}, y_{\text{corner}}) = (-L/2, L/2)$ where $L = 30$. If we start in a half-filled insulating ground state (with Fermi level $E_F = 0$), then as ϕ slides from 0 to 2π , we realize charge pumping as one corner mode merges into the occupied-state subspace while the inversion-related counterpart flows into the unoccupied-state subspace. The ground states at the two inversion-symmetric values $\phi = 0, \pi$ differ in electron number by 1, demonstrating a filling anomaly [89,90]. Because these corner modes originate as hinge modes in the 3D dimensionally promoted system (where, recall, ϕ is the momentum k_z), their existence is

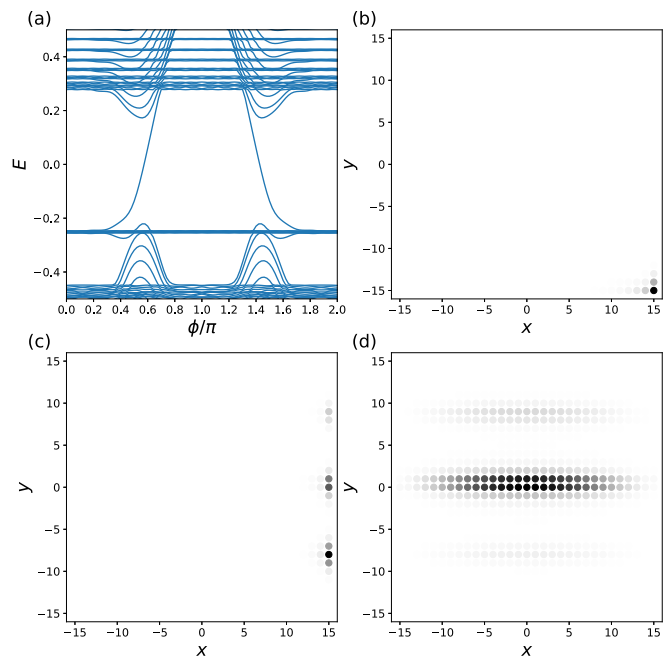


FIG. 1. (a) ϕ -sliding spectrum of the chiral 2D model in Eq. (8) with parameters given in the text. (b) Probability distribution of corner modes in the gap-crossing bands at $\phi = 0.5\pi$ and $E = -0.1368$. (c), (d) Probability distribution of edge and bulk modes at $\phi = 0.9\pi$ and $E = -0.2508$ and $E = 0.278$, respectively. The darker (black) color in (b)–(d) implies higher probability density. (b)–(d) correspond to the corner mode, edge-confined mode, and bulk-confined mode discussed in Secs. IV B–IV D, respectively. In (b)–(d), the x and y coordinates both range from $-15, \dots, +15$.

mandated by the nontrivial higher-order topology of the model Eq. (16).

By analyzing the low-energy theory of the 3D hinge modes, we will now derive the dynamics of the 2D corner modes as a function of ϕ . In 3D, the corresponding low-energy 1D hinge Hamiltonian [13,82,91] with a chiral mode as a function of k_z is given by

$$H_{\text{hinge}} = \xi v_F [k_z + 2\pi(q_x x_{\text{hinge}} + q_y y_{\text{hinge}})]. \quad (20)$$

We have assumed that for the hinge along z at position $(x_{\text{hinge}}, y_{\text{hinge}})$ there is only one chiral mode with Fermi velocity ξv_F where $v_F > 0$. We have introduced $\xi = \pm 1$ to denote whether the chiral mode has positive or negative velocity. Following our dimensional promotion procedure, Eq. (20) is then minimally coupled to a U(1) gauge field in Eq. (15) through the Peierls substitution $k_z \rightarrow k_z + 2\pi(q_x x + q_y y)$, where $x = x_{\text{hinge}}$ and $y = y_{\text{hinge}}$ are fixed.

To map Eq. (20) in 3D to the corner mode dispersion in 2D, it is helpful to first compute the ϕ -sliding spectrum for Eq. (8) with $\vec{q} = (0, 0)$, as shown in Fig. 2(a). If we identify ϕ as k_z in the hinge theory (modulo a constant offset that we will fix later), Fig. 2(a) is the \hat{z} -directed rod band structure for Eq. (16) without coupling to any vector potential. As we can see, there are linear dispersing hinge modes spanning the bulk gap, which cross each other at $k_z = \pi$. This will be used below in Eq. (21) to complete the mapping from Eq. (20) to 2D. Figure 2(a) will also serve as a reference calculation

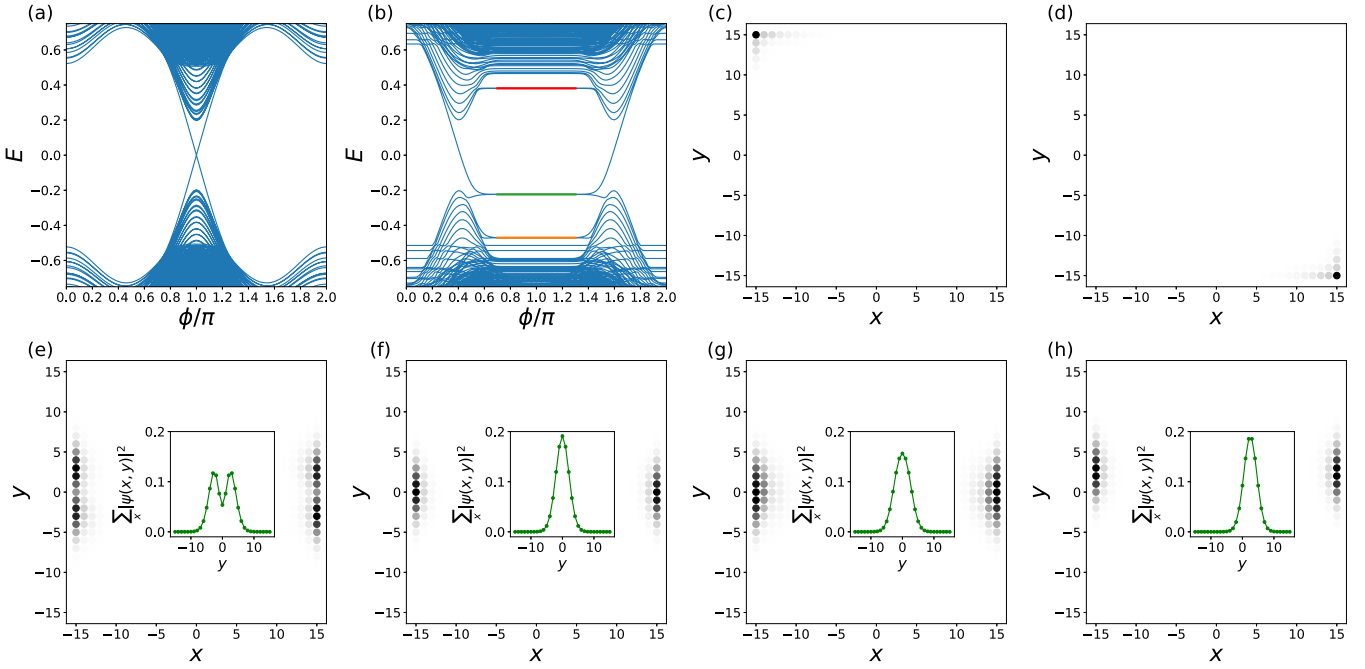


FIG. 2. (a), (b) ϕ -sliding spectrum of the chiral 2D model with the same parameters as Fig. 1(a) but with $q_y = 0$ and 0.02 , respectively. (c), (d) Probability distribution of the corner modes in (b) at $\phi = 0.4\pi$ and 1.6π and both with $E = 0.0365$. (e)–(g) Average of the probability distribution for the doubly degenerate edge-confined modes in the flat bands in (b) at $\phi = \pi$. The double degeneracy is due to the pair of opposite edges related by inversion symmetry. (e)–(g) are edge-confined modes at $\phi = \pi$ with energies $E = -0.4705$, -0.2235 , and 0.3811 , which are marked orange, green, and red, respectively, in (b). The corresponding energy eigenvalues are $E_{k_z=0, n=1}^-$, $E_{k_z=0, n=0}^-$, and $E_{k_z=0, n=1}^+$ in Eq. (28). (h) Edge-confined mode at $\phi = 0.9\pi$ with energy $E = -0.2235$ corresponding to $E_{k_z=-0.1\pi, n=0}^-$ in Eq. (28). The darker (black) color in (c)–(h) implies higher probability density. The inset in (e)–(h) is the probability distribution integrated over all x coordinates. In (c)–(h), the x and y coordinates both range from $-15, \dots, +15$.

when we examine the response of the ϕ -sliding spectrum as we increase the magnitude of \vec{q} , which will confirm our low-energy analysis.

We now use Eq. (20) to construct a low-energy description of the corner modes in Fig. 1(a) for Eq. (8). Upon projecting from 3D to 2D, the fixed hinge mode position $(x_{\text{hinge}}, y_{\text{hinge}})$ becomes the fixed corner mode position $(x_{\text{corner}}, y_{\text{corner}})$, and the hinge modes become corner modes. Since the gap-crossing modes in the $q = 0$ system shown in Fig. 2(a) intersect at $\phi = \pi$, we replace k_z in the hinge theory by $\Delta\phi = \phi - \pi$. Thus, we obtain an effective low-energy description of the corner modes as

$$H_{\text{corner}} = \xi v_F \cdot [\Delta\phi + 2\pi(q_x x_{\text{corner}} + q_y y_{\text{corner}})]. \quad (21)$$

We now verify Eq. (21) by numerically computing the ϕ -sliding spectrum shown in Fig. 2(b) with the same parameters as Fig. 1(a) but with q_y changed to 0.02 . This small value of q_y gives a smooth modulation—and hence a low flux per plaquette in the dimensionally promoted model—and is thus a suitable platform to examine the low-energy theory with minimal coupling. We observe gap-crossing modes with negative and positive slopes corresponding to corner modes at $(-L/2, L/2)$ and $(L/2, -L/2)$ where $L = 30$, respectively. These are shown in Figs. 2(c) and 2(d) at $\phi = 0.4\pi$ and 1.6π , respectively. Using Eq. (21), we have the low-energy

descriptions for these two corner modes governed by the Hamiltonians

$$H_{\text{corner } 1} = -v_F(\Delta\phi + \pi q_y L), \quad (22)$$

$$H_{\text{corner } 2} = +v_F(\Delta\phi - \pi q_y L), \quad (23)$$

where we have used $q_x = 0$. Thus, if we ramp up q_y from 0 to some nonzero value, we expect to see the corner mode dispersion shift along the ϕ axis. This is demonstrated in Fig. 2(b), which is to be compared with Fig. 2(a). In fact, a careful examination of Figs. 2(a) and 2(b) shows that the dispersions of the two corner modes shift in opposite directions as a function of $\Delta\phi$, as indicated in Eqs. (22) and (23), with the shift given by $\pi q_y L \approx 0.6\pi$ for $q_y = 0.02$ and $L = 30$. We thus see that the corner mode dispersion in Fig. 2(b) can be explained by Eq. (21). This demonstrates the origin of the corner modes in the 2D modulated system as higher dimensional hinge modes minimally coupled to a U(1) gauge field. If we consider larger q_y , such as in Fig. 1 where we have $q_y = 0.11957$, then the shift of the corner mode dispersion is predicted to be $\pi q_y L \approx 3.5871\pi$. This lies outside the first Brillouin zone and needs to be folded back into the range $\phi = [0, 2\pi)$. This occurs because, in passing from low-energy continuum theory to a lattice model, the periodicity of ϕ —which in the promoted dimension is the continuous wave number k_z —is restored. Additionally, note that Eq. (21) implies that we may tune the range of ϕ where the corner-mode energies emerge from the

bulk continuum by varying the periodicity of the modulation $\sim 1/|\bar{q}|$. As shown in Eqs. (15) and (19), tuning \bar{q} is equivalent to changing the direction and strength of the U(1) gauge field and the corresponding magnetic field in 3D.

C. Edge states

Having accounted for the low-energy description of the corner modes, we observe that in Fig. 1(a) there are additional modes with *flat dispersion*. These nondispersing modes describe states confined either to the bulk or edge of the system, as shown in Figs. 1(c) and 1(d). We now use low-energy theories to demonstrate that these states originate from the U(1) Landau quantization of the surface and bulk electrons in the promoted 3D chiral HOTI. We will revisit Figs. 1(c) and 1(d) after we complete the low-energy theory analysis using relatively small q_y .

We start with the edge-confined modes. Since a chiral HOTI can be obtained by gapping out the surface of a 3D inversion and TR-symmetric TI with a TR-breaking mass term, the generic surface theory reads [81,82,92]

$$H_{\text{surf}} = (\vec{p} \times \vec{\sigma}') \cdot \hat{n} + m\hat{n} \cdot \vec{\sigma}', \quad (24)$$

where $\vec{\sigma}'$ are Pauli matrices that act in the basis of low-energy surface states and which capture their spin and orbital texture, \vec{p} is the momentum operator, and \hat{n} is the surface normal vector. The TR operator in this surface theory is given by $\mathcal{T} = i\sigma'_y \mathcal{K}$ such that $\mathcal{T}\vec{\sigma}'\mathcal{T}^{-1} = -\vec{\sigma}'$. The momentum dependent term $(\vec{p} \times \vec{\sigma}') \cdot \hat{n}$ describes a helical surface Dirac cone, while $m\hat{n} \cdot \vec{\sigma}'$ is the TR-breaking mass term. As shown in Eq. (19), if $q_x = 0$, which is the case we consider in Figs. 1 and 2, we have that $\nabla \times \vec{A}$ is parallel to \hat{x} . We then consider a surface theory on the yz plane coupled to a perpendicular magnetic field $B\hat{x}$ generated by a Landau-gauge U(1) gauge field $\vec{A} = (0, 0, By)$. The corresponding surface Hamiltonian with the U(1) gauge field reads $H_{\text{surf}} = p_y\sigma'_y - (p_z + By)\sigma'_x + m\sigma'_x$, where we have made a Peierls substitution such that $p_z \rightarrow p_z + By$, and we have assumed that both B and m are positive. To facilitate the derivation, we perform a basis transformation through a $-2\pi/3$ radian spin rotation U along the $[1,1,1]$ axis such that $U^\dagger(\sigma'_x, \sigma'_y, \sigma'_z)U = (\sigma'_z, \sigma'_x, \sigma'_y)$. The transformed Hamiltonian then reads

$$H_{\text{surf}} = p_y\sigma'_y - (p_z + By)\sigma'_x + m\sigma'_z. \quad (25)$$

Fourier transforming Eq. (25) to replace p_z by the wave number k_z and defining a k_z -dependent ladder operator

$$a_{k_z}^\dagger = \frac{1}{\sqrt{2B}}[(k_z + By) - ip_y], \quad (26)$$

where $[a_{k_z}, a_{k_z}^\dagger] = 1$, we can rewrite Eq. (25) as

$$H_{\text{surf}}(k_z) = \begin{bmatrix} m & -\sqrt{2B}a_{k_z} \\ -\sqrt{2B}a_{k_z}^\dagger & -m \end{bmatrix}. \quad (27)$$

We can solve for the eigenstates and energy eigenvalues of Eq. (27) to find

$$\begin{aligned} \psi_{k_z, n=0}^- &= e^{ik_z z} \begin{bmatrix} 0 \\ |0, k_z\rangle \end{bmatrix}, \quad E_{k_z, n=0}^- = -m, \\ \psi_{k_z, n>0}^- &= e^{ik_z z} \begin{bmatrix} \alpha_-(n)|n-1, k_z\rangle \\ |n, k_z\rangle \end{bmatrix}, \quad E_{k_z, n>0}^- = -\sqrt{m^2 + 2Bn}, \end{aligned}$$

$$\begin{aligned} \psi_{k_z, n>0}^+ &= e^{ik_z z} \begin{bmatrix} \alpha_+(n)|n-1, k_z\rangle \\ |n, k_z\rangle \end{bmatrix}, \quad E_{k_z, n>0}^+ = +\sqrt{m^2 + 2Bn}, \\ \text{where } \alpha_\pm(n) &= \frac{-1}{\sqrt{2Bn}}(\pm\sqrt{m^2 + 2Bn} + m). \end{aligned} \quad (28)$$

Here n is a non-negative integer labeling the U(1) LLS, and $|n, k_z\rangle$ is the n th simple harmonic oscillator (SHO) eigenstate localized along y defined by the $a_{k_z}^\dagger$ in Eq. (26). Notice that the energies $E_{k_z, n=0}^-$, $E_{k_z, n>0}^-$ and $E_{k_z, n>0}^+$ of these LLS shown in Eq. (28) are all independent of k_z . As before, we now construct the low-energy description of the edge-confined modes in the 2D modulated system from the above low-energy surface theory in Eq. (25). We identify k_z in the surface theory as $\Delta\phi = \phi - \pi$, since we have flat bands as a function of ϕ in our 2D modulated system. We also identify B with $2\pi q_y$ since in our examples of Figs. 1(a) and 2(b), we have $q_x = 0$ and the corresponding vector potential is $\vec{A} = (0, 0, 2\pi q_y y)$. When we project down to the 2D model, the surface electrons correspond to states confined in the left and right edges, as shown in Figs. 1(c) and 2(e)–2(h). We again use $q_y = 0.02$ to demonstrate the low-energy theory.

We now remark on the implications of our low-energy analysis. First, the spectrum in Eq. (28) breaks particle-hole symmetry as there is a $-m$ energy eigenvalue but no $+m$ energy eigenvalue. This can be observed in Fig. 2(b), where there are no flat bands of edge-confined modes around $E \approx +0.2$, which corresponds to $E = +m$. We thus identify the flat bands in Fig. 2(b) marked by red, green, and orange as $E_{k_z, n=1}^+$, $E_{k_z, n=0}^-$, and $E_{k_z, n=1}^-$ in Eq. (28).

Second, from Eq. (28), the probability distributions for the states $\psi_{k_z, n=0}^-$ and $\psi_{k_z, n=1}^\pm$ are given by

$$|\psi_{k_z, n=0}^-|^2 \propto |\varphi_{0,B}(y + k_z/B)|^2 \quad (29)$$

$$|\psi_{k_z, n=1}^\pm|^2 \propto |\alpha_\pm(1)|^2 |\varphi_{0,B}(y + k_z/B)|^2 + |\varphi_{1,B}(y + k_z/B)|^2 \quad (30)$$

up to a normalization factor, where $\varphi_{n,B}(y)$ is the n th eigenstate of an SHO localized along y . Notice that we have indicated the explicit B dependence on $\varphi_{n,B}(y)$ since the cyclotron frequency and the localization of the wave function depend on the strength of magnetic field. This implies that $\psi_{k_z, n=0}^-$ has a pure Gaussian distribution. Furthermore, we expect that $\psi_{k_z, n=1}^-$ is more characteristic of an SHO first excited state than $\psi_{k_z, n=1}^+$ since $|\alpha_-(1)|^2 = (-\sqrt{m^2 + 2B} + m)^2 / (2B) < (\sqrt{m^2 + 2B} + m)^2 / (2B) = |\alpha_+(1)|^2$, as we have assumed both B and m are positive. Figures 2(e)–2(g) show the 2D wave function probability distributions at $\phi = \pi$ for edge confined modes in different LLS in our lattice model, together with the insets showing the integrated wave function probability over all x coordinates. While both Figs. 2(e) and 2(g) correspond to $n = 1$ LL, the former is at the negative energy branch and the latter is at the positive energy branch. Therefore Fig. 2(e) shows split peaks characteristic of the SHO first excited state, more so than Fig. 2(g). In contrast, Fig. 2(f), corresponding to the $n = 0$ LL wave function, shows the Gaussian probability distribution characteristic of the SHO ground state. We see that the qualitative properties of the wave functions are all consistent with the low-energy surface theory.

Third, the definition of the ladder operator in Eq. (26) implies that the center of the wave functions will be shifted by $-k_z/B$ from $y = 0$. Identifying k_z in the low-energy theory as $\Delta\phi = \phi - \pi$ and B as $2\pi q_y$, we deduce that the distance l that the edge-confined mode gets shifted along y in the lattice model will be $l = -\Delta\phi/(2\pi q_y)$. Notice that the edge-confined mode in Fig. 2(h) at $\phi = 0.9\pi$ ($\Delta\phi = -0.1\pi$) is shifted by $\approx +2.5$ lattice constants along y comparing with Fig. 2(f), which is at $\phi = \pi$ ($\Delta\phi = 0$). This is consistent with our prediction, as l will be $+2.5$ when $\Delta\phi = -0.1\pi$ and $q_y = 0.02$.

Fourth, although Eq. (28) predicts nondegenerate energy levels for a single surface with a perpendicular U(1) magnetic field, in Fig. 1(a) the flat band corresponding to the $E_{k_z, n=0}^-$ level is highly degenerate. This is due to zone-folding effects, similar to what we observed for the corner mode dispersion in Fig. 1(a). As the gap-crossing modes are shifted outside $\phi = [0, 2\pi)$, they get folded back to $\phi = [0, 2\pi)$ together with the flat bands connected to them. Up to the degeneracy due to zone folding, the universal feature is that the edge-confined modes appearing in our 2D chiral DW system originate from the projection of surface electrons in a chiral HOTI with U(1) Landau quantization.

Before moving on, let us remark on the robustness of our low-energy predictions to perturbations of the model. If we consider a more complicated modulated system with, for example, long-range and anisotropic hopping terms together with other on-site potentials, as long as the promoted 3D system still preserves inversion symmetry and the gap is not closed, the 3D system will still be in the same chiral HOTI phase. However, the low-energy theories that we have constructed might be modified. For example, the low-energy theory at the surfaces, which we model with Eq. (25), may be modified as

$$H_{\text{surf}} = \alpha_y p_y \sigma'_y - \alpha_z (p_z + By) \sigma'_x + m \sigma'_z + \Delta \sigma'_0 + O(p_y^2, p_z^2, p_y p_z). \quad (31)$$

Differences between α_x and α_y can lead to an anisotropic gapped Dirac cone. A nonzero Δ induces unequal masses in different subspace of $\vec{\sigma}'$ which can shift the entire energy spectrum. $O(p_y^2, p_z^2, p_y p_z)$ represents higher-order terms in the low-energy theory which might cause nonlinearity in the band dispersion in Eq. (31) without minimal coupling. By the same reasoning, we might also have nonlinear hinge mode energies with a quadratic momentum correction in Eq. (20). All of

these additional terms will change the energetic feature of the system, such as energy spectra, Fermi velocities, together with the detailed form of the wave functions, which will be inevitably different from Eq. (28). Nevertheless, the following features are universal: (1) There will be electrons confined to the surface that undergo U(1) Landau quantization, and therefore there will be states that are confined along some directions. Upon projecting down to the 2D modulated system, we will still obtain edge-confined modes. (2) There will be (non)linear hinge mode dispersion that will be shifted along k_z due to the minimal coupling. Therefore, the statement that we can tune the range of ϕ where the gap-crossing corner modes appear by tuning the magnitude of the modulation wave vectors, will still hold. We use the low-energy theories Eqs. (20) and (25) since these allow us to uncover the relation between the states in the promoted dimension and those in the original low-dimensional modulated system in an analytically tractable way.

D. Bulk states

The above analysis on corner- and edge-confined modes shows that the corresponding higher dimensional description of our modulated system is a 3D chiral HOTI minimally coupled to a U(1) gauge field. To complete our analysis, we will now focus on the bulk states. As expected, the low-energy description of the bulk-confined modes, shown in Fig. 1(d), will correspond to the low-energy theory of bulk electrons in a 3D chiral HOTI minimally coupled to a U(1) gauge field. We start with the Bloch Hamiltonian of the promoted 3D chiral HOTI [Eq. (16) with $q_x = q_y = 0$] expanded around the Γ point [88]:

$$H_{\text{bulk}} = m_{\text{bulk}} \tau_z \sigma_0 + \tau_x \vec{p} \cdot \vec{\sigma} + \tau_0 \vec{M} \cdot \vec{\sigma}. \quad (32)$$

We have defined several parameters to make Eq. (32) compact for later convenience, and introduced $\tau_0 \vec{M} \cdot \vec{\sigma}$ where $\vec{M} = (M, M, M)$ corresponds to the ferromagnetic potential in Eq. (10). We now couple this H_{bulk} to $\vec{A} = By\hat{z}$, which is equivalent to Eq. (15) with $q_x = 0$. This can be done via the minimal substitution $p_z \rightarrow p_z + By$. Fourier transforming along x and z to replace p_x and p_z by wave numbers k_x and k_z , and defining the k_z -dependent ladder operator as

$$a_{k_z}^\dagger = \frac{1}{\sqrt{2B}} (k_z + By - ip_y), \quad (33)$$

we can rewrite Eq. (32) coupled to $\vec{A} = By\hat{z}$ in terms of a_{k_z} and $a_{k_z}^\dagger$ as

$$H_{\text{bulk}}(k_x, k_z) = m_{\text{bulk}} \tau_z \sigma_0 + \tau_x \begin{bmatrix} \sqrt{\frac{B}{2}} (a_{k_z} + a_{k_z}^\dagger) & k_x - \sqrt{\frac{B}{2}} (a_{k_z} - a_{k_z}^\dagger) \\ k_x + \sqrt{\frac{B}{2}} (a_{k_z} - a_{k_z}^\dagger) & -\sqrt{\frac{B}{2}} (a_{k_z} + a_{k_z}^\dagger) \end{bmatrix} + \tau_0 \vec{M} \cdot \vec{\sigma}. \quad (34)$$

We have numerically shown in the SM [58] that the effective theory in Eq. (34) captures several properties of the flat bulk bands in Fig. 2(b) with relatively small $q_y = 0.02$, such as energy asymmetry with respect to $E = 0$ and the

confinement direction of the bulk states due to U(1) Landau quantization.

From the above analysis on corner-, edge-, and bulk-confined modes, we conclude that we can characterize this

topological 2D modulated system with chiral sliding modes in terms of a 3D chiral HOTI coupled to a U(1) gauge field. In addition, such 2D modulated systems provide a platform to examine the properties of a 3D chiral HOTI by sliding the DW order parameter ϕ .

V. HELICAL HIGHER-ORDER SLIDING MODES AND SU(2) GAUGE FIELDS

Next, we will generalize our formalism to TR invariant spinful systems. In doing so, we will see that incommensurate modulations induce coupling to SU(2) gauge fields in the dimensionally promoted models. SU(2) gauge fields can be used to represent spin-orbit coupling [93], which is ubiquitous in topological states of matter. For example, SU(2) gauge fields in 3D and 4D generates SU(2) LLs that give rise to 3D TIs and 4D QHEs [94,95]. A non-Abelian SU(2) Peierls phase in 2D and 3D lattices can also lead to 2D and 3D TIs [93,96]. In addition, in response to a bulk SU(2) gauge flux insertion, a 2D TI can bind various quasiparticle excitations such as spinons, holons, and chargeons [97]. In this section, we present a 2D modulated system that allows us to simulate a 3D helical HOTI coupled to an SU(2) gauge field.

A. Dimensionally promoted helical model

We start by considering the following 2D Hamiltonian on a square lattice with one modulated on-site potential [$V(\vec{q}, \vec{n}, \phi)$]:

$$H = \sum_{\vec{n}} \psi_{\vec{n}+\hat{x}}^\dagger [H_{+\hat{x}}] \psi_{\vec{n}} + \psi_{\vec{n}+\hat{z}}^\dagger [H_{+\hat{z}}] \psi_{\vec{n}} + \text{H.c.} + \sum_{\vec{n}} \psi_{\vec{n}}^\dagger ([H_{\text{on-site}}] + [V(\vec{q}, \vec{n}, \phi)]) \psi_{\vec{n}}, \quad (35)$$

where the unmodulated couplings are

$$[H_{+\hat{x}}] = \frac{v_x}{2} \tau_z \mu_0 \sigma_0 - \frac{u_x}{2i} \tau_y \mu_y \sigma_0, \quad (36)$$

$$[H_{+\hat{z}}] = \frac{v_z}{2} \tau_z \mu_0 \sigma_0 - \frac{u_z}{2i} \tau_x \mu_x \sigma_0, \quad (37)$$

$$[H_{\text{on-site}}] = m_1 \tau_z \mu_0 \sigma_0 + m_2 \tau_z \mu_x \sigma_0 + m_3 \tau_z \mu_z \sigma_0 + m_{v_1} \tau_0 \mu_z \sigma_0 + m_{v_2} \tau_0 \mu_x \sigma_0. \quad (38)$$

The matrices $\vec{\tau}$, $\vec{\mu}$, and $\vec{\sigma}$, are Pauli matrices and denote the orbital, sublattice, and spin degrees of freedom, respectively. The hopping matrices $[H_{+\hat{x}}]$ and $[H_{+\hat{z}}]$, together with the on-site potential $[H_{\text{on-site}}]$ respect both inversion and TR symmetries. The inversion and TR operations are represented by τ_z and $i\tau_z \sigma_y \mathcal{K}$, respectively [84]. These hoppings give rise to low-energy four-component Dirac fermions in each spin subspace, realizing a topological critical point. The modulated on-site energy is given by

$$[V(\vec{q}, \vec{n}, \phi)] = v_y \tau_z \mu_0 \begin{bmatrix} \cos \theta_{\vec{q}, \vec{n}, \phi}^+ & 0 \\ 0 & \cos \theta_{\vec{q}, \vec{n}, \phi}^- \end{bmatrix} + v_H \tau_y \mu_z \begin{bmatrix} \sin \theta_{\vec{q}, \vec{n}, \phi}^+ & 0 \\ 0 & \sin \theta_{\vec{q}, \vec{n}, \phi}^- \end{bmatrix}, \quad (39)$$

where $\theta_{\vec{q}, \vec{n}, \phi}^\pm = 2\pi \vec{q} \cdot \vec{n} \pm \phi$, $\vec{q} = (q_x, q_z)$ is the modulation wave vector in 2D, $\vec{n} \in \mathbb{Z}^2$ is the lattice position and ϕ is the sliding phase. The first term in Eq. (39) modulates the mass $m_1 \tau_z \mu_0 \sigma_0$ in Eq. (38), which may represent unequal on-site energy for s and p orbitals, with forward ($-\phi$) and backward ($+\phi$) sliding phases in each spin subspace [96,98]. The second term in Eq. (39) describes a modulation of the on-site energy which mixes s and p orbitals with unequal strength for different sublattices. Similarly, we have forward and backward sliding phases in different spin subspaces for the second term. Since the modulation in Eq. (39) has opposite phase offsets in each spin subspace, it may be induced from spin-orbit coupled spin ordering. This modulation is TR and inversion symmetric only when $\phi = 0, \pi$. Note, however, that the product of inversion and TR symmetry, which we will denote \mathcal{IT} symmetry, is preserved for all values of ϕ . If we denote the third, synthetic dimension as y , this 2D model is equivalent to the inversion and TR symmetric 3D helical HOTI model of Ref. [84], coupled to an SU(2) gauge field given by

$$\vec{A} = (0, 2\pi(q_x x + q_z z)\sigma_z, 0). \quad (40)$$

This matrix-valued \vec{A} produces a constant SU(2) magnetic field [99] $\vec{B} = \nabla \times \vec{A} - i\vec{A} \times \vec{A}$, determined from the field strength [100] $F_{\mu\nu} = \partial_\mu A_\nu - \partial_\nu A_\mu - i[A_\mu, A_\nu]$, and given by

$$\vec{B} = (-2\pi q_z \sigma_z, 0, 2\pi q_x \sigma_x). \quad (41)$$

This constant SU(2) field strength preserves both inversion and TR symmetry in 3D, up to a spin-dependent gauge transformation (see SM [58]). Notice that Eq. (41) implies that the SU(2) magnetic field in this example can be interpreted as a U(1) magnetic field with opposite sign for spin-up and spin-down electrons [96,98]. We then expect that, for a suitable choice of parameters such that the SU(2) gauge field does not close the bulk gap in 3D, the insulating ground state will be in the same nontrivial helical HOTI phase as the model with $\vec{q} = 0$ [13,14,82]. Therefore, in 3D, our promoted model will support an odd number of pairs of sample-encircling helical hinge modes respecting inversion and TR symmetries [82,84]. Upon being projected back to 2D, the helical hinge modes in 3D become \mathcal{IT} -related pairs of corner modes at the same ϕ in the 2D modulated system. In the SM [58], we give the form of the 3D dimensionally promoted model in position space.

B. Calculation of the spectrum

Let us now numerically verify these conclusions. Figure 3(a) shows the ϕ -sliding spectrum of Eq. (35) with parameters $m_1 = -3$, $m_2 = 0.3$, $m_3 = 0.2$, $m_{v_1} = -0.4$, $m_{v_2} = 0.2$, $v_x = v_z = u_x = u_z = 1$, $v_y = 2$, $v_H = 1.2$ [84], and $\vec{q} = (0, q_z)$, where $q_z = 0.11957$ [36]. The system size is 31×31 . There are doubly degenerate pairs of states which cross the gap as a function of ϕ , where the degeneracy is protected by \mathcal{IT} symmetry. We see from the wave functions that these are corner modes related by \mathcal{IT} symmetry, as shown in Fig. 3(b) for the branch with negative slope around $\phi \approx 0.4\pi$. In the other branch of doubly degenerate gap-crossing states with positive slope, the corner modes are the inversion-symmetric counterpart (where recall that inversion symmetry leaves spin invariant) to those in Fig. 3(b). Therefore, as ϕ slides from

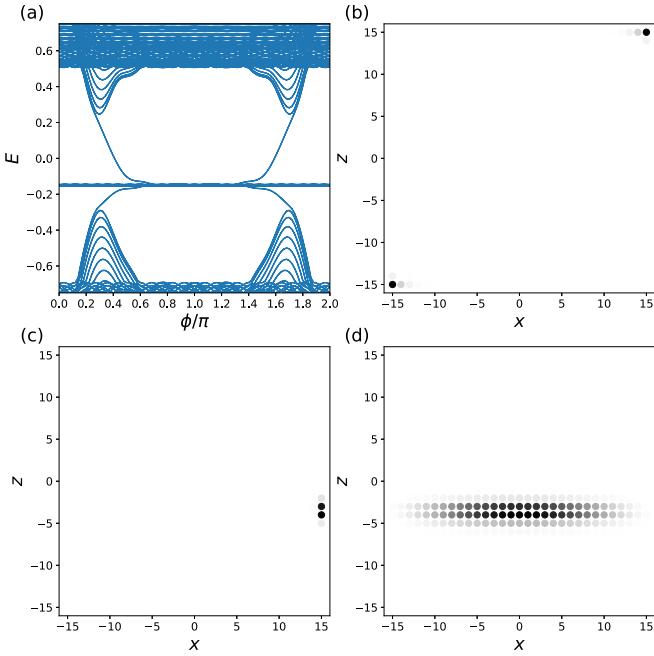


FIG. 3. (a) ϕ -sliding spectrum of the 2D helical model in Eq. (35) with parameters given in the text. (b) Summation of the probability density of the doubly degenerate corner modes at $\phi = 0.4\pi$ and $E = 0.0146$. The two corner modes at the same ϕ are related to each other by the \mathcal{IT} symmetry, and hence they are localized at inversion-related corners and have opposite spins. (c), (d) Probability distribution of edge and bulk modes at $\phi = 0.9\pi$ and $E = -0.1459$ and $E = 0.5227$, respectively. The darker (black) color in (b)–(d) implies higher probability density. In (b)–(d), the x and z coordinates both range from $-15, \dots, +15$.

0 to 2π , this model realizes a \mathbb{Z}_2 pump [101,102] as one of the pairs of corner states will merge into the occupied-state subspace (with Fermi level $E_F = 0$) while the other pair will flow out. In our specific examples, the two states in each \mathcal{IT} -related pair at the same ϕ are spin eigenstates and, therefore, in this case the \mathbb{Z}_2 pump is a spin pump; our conclusions, however, hold even when spin is not conserved.

As mentioned earlier, and in analogy with our chiral HOTI model, the corner modes here are equivalent to hinge modes along y in 3D. The corresponding low-energy theory for these corner modes is

$$H_{\text{corner}} = v_F [\phi \sigma'_z + 2\pi (q_x x_{\text{corner}} + q_z z_{\text{corner}}) \sigma'_0], \quad (42)$$

where v_F is the group velocity of the hinge modes in 3D. We use the Pauli matrices $\vec{\sigma}'$ to denote the effective basis where in each subspace the states have opposite spins together with some orbital and sublattice textures. We have assumed without loss of generality that there is only one pair of helical hinge modes at the hinge along y in the promoted 3D system. By denoting ϕ as k_y , which is the crystal momentum along y , we recognize Eq. (42) as the hinge mode dispersion $H(k_y) = v_F k_y \sigma'_z$ in 3D minimally coupled to an $SU(2)$ gauge field described by Eq. (40). Similar to Sec. IV, as we vary \vec{q} —which is equivalent to changing the strength and (spatial) direction of the $SU(2)$ gauge field in Eqs. (40) and (41)—the dispersion of the spin-polarized corner modes will shift along

the ϕ axis. In the SM [58], we present a complete low-energy theory analysis for the corner modes with the same structure as Sec. IV.

In addition, we show in Figs. 3(c) and 3(d) the probability density for the edge- and bulk-confined modes in the flat bands of Fig. 3(a). Similar to the corner modes, these can be, respectively, understood in terms of 3D low-energy surface and bulk theories minimally coupled to an $SU(2)$ gauge field, leading to an $SU(2)$ Landau quantization [93,94]. The relevant surface theory describes a time-reversed pair of Chern insulators (CIs). The relevant bulk theory is the $\vec{k} \cdot \vec{p}$ expansion around Γ of the promoted 3D helical HOTI Hamiltonian [84]. We provide further details in the SM [58]. Together with the corner mode analysis, we see that this topological 2D modulated system with helical sliding modes can be characterized by a 3D lattice model coupled to an $SU(2)$ gauge field. In addition, we have shown how 2D modulated systems can provide a platform to examine $SU(2)$ gauge physics in higher dimensions, by sliding the phase ϕ of the DW order parameter.

VI. WEYL-CDWs AND 4D TOPOLOGICAL MODES

As a final demonstration of our dimensional promotion formalism and its utility to investigating physics in more than 3D, we consider the mean-field state of a correlated inversion-symmetric 3D WSM with CDW distortion (Weyl-CDW) [30,35,36,53,103–106]. It has been shown that such a system can realize various topological phases. Depending on the phase ϕ of the CDW order parameter, the system can interpolate between QAH and *obstructed* QAH (oQAH) phase [53]. This is due to the $\pi \bmod 2\pi$ axion angle difference $\delta\theta_\phi = \theta(\phi = \pi) - \theta(\phi = 0)$ for the system with $\phi = 0$ and $\phi = \pi$ in the thermodynamic limit. Physically, this leads to a Hall conductance difference

$$|G_{xy}(\phi = \pi) - G_{xy}(\phi = 0)| = e^2/h \bmod 2e^2/h \quad (43)$$

for a semi-infinite slab (see also Eq. (61) below, as well as Refs. [107,108]). In this section, we analyze a minimal model of a 3D inversion-symmetric magnetic Weyl-CDW system, which admits a dimensional promotion to 4D with a $U(1)$ gauge field. We will explain the origin of the background QAH response and the interpolation between QAH and oQAH phases using the corresponding 4D theory. In the following, we will denote a sample infinite along x and y with finite thickness L_z along the z direction as an xy slab. Similarly, we will use the term y rod to denote a sample infinite along y and finite along x and z with size $L_x \times L_z$.

A. 3D Weyl-CDW model and dimensional promotion

To begin, we consider electrons on a 3D cubic lattice with Hamiltonian $H = H_0 + H_{\text{CDW}}(\phi)$. Here H_0 is a periodic tight-binding Hamiltonian given by

$$\begin{aligned} H_0 = & \left(\sum_{\vec{n}} [-it_x \psi_{\vec{n}+\hat{x}}^\dagger \sigma_x \psi_{\vec{n}} - it_y \psi_{\vec{n}+\hat{y}}^\dagger \sigma_y \psi_{\vec{n}} + t_z \psi_{\vec{n}+\hat{z}}^\dagger \sigma_z \psi_{\vec{n}}] \right. \\ & + \sum_{\vec{n}} \frac{m}{2} (\psi_{\vec{n}+\hat{x}}^\dagger \sigma_z \psi_{\vec{n}} + \psi_{\vec{n}+\hat{y}}^\dagger \sigma_z \psi_{\vec{n}} - 2\psi_{\vec{n}}^\dagger \sigma_z \psi_{\vec{n}}) \\ & \left. - \sum_{\vec{n}} t_z (\cos(\pi q)) \psi_{\vec{n}}^\dagger \sigma_z c_{\vec{n}} \right) + \text{H.c.} \end{aligned} \quad (44)$$

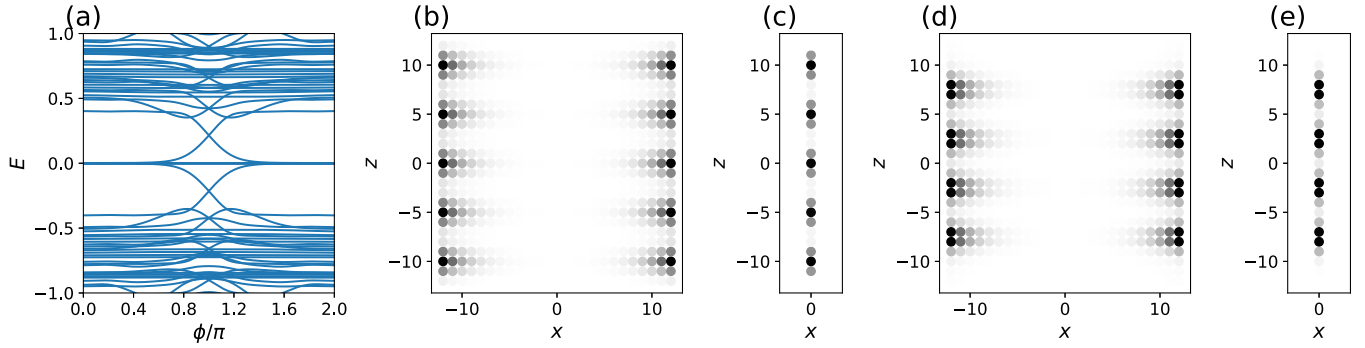


FIG. 4. (a) ϕ -sliding spectrum of the Weyl-CDW model in a y rod geometry at $k_y = 0$ with size $L_x \times L_z = 25 \times 25$, $t_x = -t_y = t_z = 1$, $m = 2$, $2|\Delta| = 0.75$, and $q = 1/5$. (b) The average probability distribution of the ten zero modes at $\phi = 0$ in (a). These zero modes correspond to QAH surface states. (c) The average probability distribution of the five nontrivial states at $\vec{k} = \Gamma$ of the xy slab at $\phi = 0$, which in total lead to $G_{xy}(\phi = 0) = -5e^2/h$. (d) The average probability distribution of the eight zero modes at $\phi = \pi$ in (a). These zero modes correspond to QAH surface states. (e) The average probability distribution of the four nontrivial states at $\vec{k} = \Gamma$ of the xy slab at $\phi = \pi$, which in total lead to $G_{xy}(\phi = \pi) = -4e^2/h$. The darker (black) color in (b)–(e) implies higher probability density. In (b) and (d), the x and z coordinates both range from $-12, \dots, +12$. In (c) and (e), the z coordinate ranges from $-12, \dots, +12$.

in position space. The corresponding Bloch Hamiltonian is

$$H_0(\vec{k}) = -2[t_x \sin(k_x)\sigma_x + t_y \sin(k_y)\sigma_y] - m[2 - \cos(k_x) - \cos(k_y)]\sigma_z + 2t_z[\cos(k_z) - \cos(\pi q)]\sigma_z, \quad (45)$$

with $m/2 \geq t_x, -t_y, t_z > 0$. We take for the on-site modulation

$$H_{\text{CDW}}(\phi) = 2|\Delta| \sum_{\vec{n}} \cos(2\pi q n_z + \phi) \psi_{\vec{n}}^\dagger \sigma_z \psi_{\vec{n}}. \quad (46)$$

Here $2|\Delta|$ is the strength of the CDW modulation, $2\pi q$ is the magnitude of the modulation wave vector $2\pi \vec{q} = (0, 0, 2\pi q)$, and ϕ is the phase of CDW order parameter. We again use $\vec{\sigma}$ to denote the Pauli matrices, which here index an orbital degree of freedom. The inversion and TR operation are represented by σ_z and \mathcal{K} , respectively (note that this is a model of spinless electrons). The Hamiltonian H_0 then describes a TR-breaking, inversion-symmetric magnetic WSM with Weyl nodes at $\vec{k} = (0, 0, \pm\pi q)$, see Eq. (45) [109]. The perturbation $H_{\text{CDW}}(\phi)$ is the CDW modulation that couples these two Weyl nodes and opens a gap in the bulk spectrum [53]. Note that in this simple model, we have chosen the modulation wave vector to be exactly equal to the Weyl node separation vector for simplicity of analysis. Even though the bulk is gapped, the surface of this 3D Weyl-CDW is gapless, due to the presence of QAH surface states. In Fig. 4(a), we show the ϕ -sliding spectrum for a y rod of $H_0 + H_{\text{CDW}}(\phi)$ at $k_y = 0$ with size $L_x \times L_z = 25 \times 25$, $t_x = -t_y = t_z = 1$, $m = 2$, $2|\Delta| = 0.75$ and $q = 1/5$. This corresponds to a commensurate Weyl-CDW system. The midgap zero modes in Fig. 4(a) correspond to the QAH surface states. In Fig. 4(b), we show the probability distribution of the ten zero modes at $\phi = 0$. Together with Wilson loop and Berry curvature calculation in the SM [58], we verify that the corresponding xy slab with $L_z = 25$ carries a slab Hall conductance $G_{xy}(\phi = 0) = -5e^2/h$. We can then identify the weak Chern number [10, 110–112] of the 3D periodic system with $5 = 25/5$ unit cells (since $q = 1/5$) as $\nu_z = -1$.

As in Secs. IV and V, we identify ϕ with the crystal momentum k_w along a fourth, synthetic direction denoted by

w . Using the dimensional promotion procedure in Sec. III, we can promote $H_0 + H_{\text{CDW}}(\phi)$ to a 4D nodal line system coupled to a U(1) gauge field. In the SM [58], we give the explicit form of the promoted model in 4D position space. The corresponding 4D nodal line system (with $q = 0$) has a Bloch Hamiltonian:

$$H(\vec{k}) = -2[t_x \sin(k_x)\sigma_x + t_y \sin(k_y)\sigma_y] + 2|\Delta| \cos(k_w)\sigma_z - m[2 - \cos(k_x) - \cos(k_y)]\sigma_z + 2t_z[\cos(k_z) - \cos(\pi q)]\sigma_z. \quad (47)$$

The spectrum of this Hamiltonian features nodal lines at $k_x = k_y = 0$ defined by the implicit equation

$$t_z \cos(k_z) + |\Delta| \cos(k_w) = t_z \cos(\pi q). \quad (48)$$

According to Eq. (6), we then couple this Hamiltonian to a 4D U(1) gauge field given by

$$\vec{A} = (0, 0, 0, 2\pi qz), \quad (49)$$

since $2\pi \vec{q} = 2\pi q\hat{z}$ in this system. This \vec{A} only produces nonzero field strength threading the zw plane,

$$F_{zw} = -F_{wz} = \partial_z A_w - \partial_w A_z = 2\pi q, \quad (50)$$

where all other components of $F_{\mu\nu} = \partial_\mu A_\nu - \partial_\nu A_\mu$ are zero. We are now in a position to reinterpret the existence of a background QAH response and QAH surface states when the bulk gap is opened due to the CDW. We will see how these features emerge from the low-energy approximation for this 4D system minimally coupled to Eq. (49).

B. Low-energy theory analysis

We start from the 4D Bloch Hamiltonian in Eq. (47). Expanding around $\vec{k} = \vec{0}$, we have

$$H(\vec{k}) \approx -2[t_x k_x \sigma_x + t_y k_y \sigma_y] + 2t_z \left(1 - \frac{k_z^2}{2} - \cos(\pi q)\right) \sigma_z + 2|\Delta| \left(1 - \frac{k_w^2}{2}\right) \sigma_z. \quad (51)$$

The nodal line in this low-energy theory is an ellipse in the k_z - k_w plane with $k_x = k_y = 0$, defined by

$$t_z k_z^2 + |\Delta| k_w^2 = 2t_z[1 - \cos(\pi q)] + 2|\Delta| > 0. \quad (52)$$

Replacing the 4D wave vector $\vec{k} = (k_x, k_y, k_z, k_w)$ by the 4D momentum operator $\vec{p} = (p_x, p_y, p_z, p_w)$ using the so-called envelope function approximation [8,91,113–118], the Hamiltonian governing the low-energy dynamics reads

$$H = -2[t_x p_x \sigma_x + t_y p_y \sigma_y] + 2t_z \left(1 - \frac{p_z^2}{2} - \cos(\pi q)\right) \sigma_z + 2|\Delta| \left(1 - \frac{p_w^2}{2}\right) \sigma_z. \quad (53)$$

Next, let us minimally couple Eq. (53) to a 4D U(1) gauge field $\vec{A} = (0, 0, 0, 2\pi qz)$ via a Peierls substitution such that $p_w \rightarrow p_w + 2\pi qz$. Equation (53) then becomes

$$H = -2[t_x p_x \sigma_x + t_y p_y \sigma_y] + 2(t_z[1 - \cos(\pi q)] + |\Delta|) \sigma_z - (t_z p_z^2 + |\Delta|(p_w + 2\pi qz)^2) \sigma_z, \quad (54)$$

where we have assumed that the particle carries -1 charge. Fourier transforming along x , y , and w , we may replace p_x , p_y , and p_w by the corresponding wave numbers k_x , k_y , k_w , such that

$$H(k_x, k_y, k_w) = -2[t_x k_x \sigma_x + t_y k_y \sigma_y] + 2(t_z[1 - \cos(\pi q)] + |\Delta|) \sigma_z - (t_z p_z^2 + |\Delta|(k_w + 2\pi qz)^2) \sigma_z. \quad (55)$$

Notice that the coefficient of σ_z in the final term in the Hamiltonian,

$$t_z p_z^2 + |\Delta|(k_w + 2\pi qz)^2, \quad (56)$$

is an SHO Hamiltonian along z which can be diagonalized as

$$4\pi q \sqrt{t_z |\Delta|} \left(n + \frac{1}{2}\right). \quad (57)$$

Here n is a non-negative integer and the eigenvalue of the number operator $a_{k_w, q}^\dagger a_{k_w, q}$ with

$$a_{k_w, q}^\dagger = \frac{1}{\sqrt{4\pi q}} \left(\frac{t_z}{|\Delta|}\right)^{\frac{1}{4}} \left[\left(\frac{|\Delta|}{t_z}\right)^{\frac{1}{2}} (k_w + 2\pi qz) - ip_z \right]. \quad (58)$$

The quantum number n is the 4D U(1) LL index. By restricting to a subspace of the full Hilbert space with fixed n and k_w , we see that the 4D low-energy Hamiltonian Eq. (54) may be decomposed into a direct sum of 2D low-energy CIs in xy plane parameterized by n and k_w . The Hamiltonian for these 2D CIs is given by

$$H_{2D \text{ CI}}(n, k_w) = -2[t_x p_x \sigma_x + t_y p_y \sigma_y] + 2m \sigma_z, \quad (59)$$

where

$$m = t_z(1 - \cos(\pi q)) + |\Delta| - 2\pi q \sqrt{t_z |\Delta|} \left(n + \frac{1}{2}\right). \quad (60)$$

Since we have restricted to the subspace with fixed n and k_w in Eq. (59), according to Eq. (56) the wave function along z and w will be SHO eigenstates centered at $z = -k_w/(2\pi q)$

multiplied by a plane wave $e^{ik_w w}$. Notice that the k_w dependence of Eq. (59) is due to the integer n in Eq. (60), which is an eigenvalue of the number operator $a_{k_w, q}^\dagger a_{k_w, q}$. Therefore, the eigenstates in the low-energy approximation take the form of plane waves in w , and CI eigenstates as a function of (x, y) localized at different constant- z planes for different k_w . This provides a 4D interpretation of the layer construction of the Weyl-CDW presented in Refs. [53,103].

As in a 3D nodal ring system with a perpendicular magnetic field [119], Eq. (59) can yield a gapped 4D bulk spectrum provided that $m \neq 0 \forall n \geq 0$. This insulating ground state will then carry nontrivial topology inherited from the nodal line system, since in Eq. (59) we found that the gapped 4D continuum theory is composed of low-energy 2D CIs. We then expect that there will be CI layers in the xy plane of the corresponding 4D lattice model (see SM [58]). The CI layers will also be separated along z by $2\pi/(2\pi q) = 1/q$ for a fixed k_w , due to the 2π periodicity of k_w in the lattice model. In our current example, this separation is 5 since $q = 1/5$. Notice that k_w is now interpreted as the crystal momentum along the fourth dimension. To connect these observation in 4D back to the physical 3D Weyl-CDW system with Hamiltonian $H_0 + H_{\text{CDW}}(\phi)$, we notice that each 3D Weyl-CDW system with a fixed ϕ corresponds to the 4D theory with a fixed k_w . Focusing on the xy slab with $\phi = 0$ and thickness $L_z = 25$, in which $G_{xy}(\phi = 0) = -5e^2/h$, we show wave functions corresponding to the only 5 layers of nontrivial CIs separated from each other by five lattice constants along z in Fig. 4(c). Each of these CI layers carries Chern number $C = -1$ and contributes one chiral edge mode along y in the y rod, shown in Fig. 4(b). In the SM [58], we provide technical details on identifying the nontrivial CI layers using hybrid Wannier function, Berry phases, and Berry curvature calculations for an xy slab. We can thus regard the CDW-induced gap opening and the existence of background QAH response as the results of U(1) Landau quantization in the 4D nodal line system.

Next, we address the interpolation between the QAH phase at $\phi = k_w = 0$ and the oQAH phase at $\phi = k_w = \pi$ using the 4D theory. Before we turn to the 4D low-energy theory, we begin with the observation that in Fig. 4(a), the number of midgap zero modes corresponding to QAH surface states decreases by 2 as ϕ slides from 0 to π ; one state is lowered into the valence band, while one state is elevated to the conduction band. This is consistent with the change in Hall conductance Eq. (43), which is derived in the thermodynamic limit where the 2D slab thickness $L_z \rightarrow \infty$ with infinitesimal but nonzero $2|\Delta|$ [53]. The ambiguity modulo $2e^2/h$ in the change of Hall conductance is due to the axion angle θ , which is only well-defined mod 2π , as shown below in Eq. (61). Taking $L_z \rightarrow \infty$ with infinitesimal $2|\Delta|$ ensures that the only effect the CDW modulation has is to open the gap at the Weyl points without inverting bands at other high-symmetry points in the 3D Brillouin zone. We have also verified that our choice for the parameters in Fig. 4(a) is adiabatically connected to this condition by increasing L_z and decreasing $2|\Delta|$. The slab Hall conductance G_{xy} of the xy slab contains both an extensive contribution from the bulk QAH phase through the weak Chern number ν_z , and an intensive

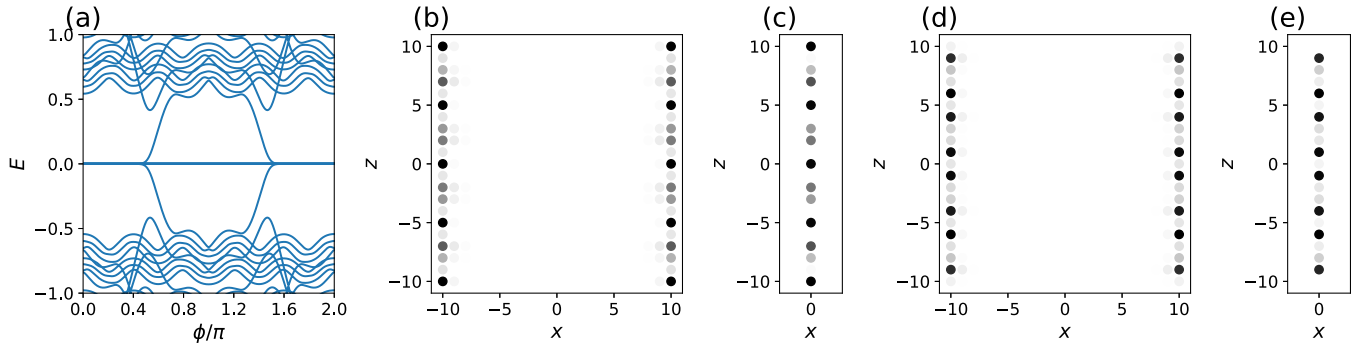


FIG. 5. (a) ϕ -sliding spectrum of the Weyl-CDW model in a y rod geometry at $k_y = 0$ with size $L_x \times L_z = 21 \times 21$, $t_x = -t_y = t_z = 1$, $m = 2$, $2|\Delta| = 2$, and $q = \tau/4$ where $\tau = (1 + \sqrt{5})/2$. (b) The average probability distribution of the 18 zero modes at $\phi = 0$ in (a). These zero modes correspond to QAH surface states. (c) The average probability distribution of the nine nontrivial states at $\vec{k} = \Gamma$ of the xy slab at $\phi = 0$, which in total lead to $G_{xy}(\phi = 0) = -9e^2/h$. (d) The average probability distribution of the 16 zero modes at $\phi = \pi$ in (a). These zero modes correspond to QAH surface states. (e) The average probability distribution of the eight nontrivial states at $\vec{k} = \Gamma$ of the xy slab at $\phi = \pi$, which in total lead to $G_{xy}(\phi = \pi) = -8e^2/h$. The darker (black) color in (b)–(e) implies higher probability density. In (b) and (d), the x and z coordinates both range from $-10, \dots, +10$. In (c) and (e), the z coordinate ranges from $-10, \dots, +10$.

contribution from axion angle θ , which collectively gives [92,108]

$$G_{xy} = \frac{e^2}{h}(v_z l_z + \theta/\pi), \quad (61)$$

where l_z is the number of unit cells in the slab. In our examples for $q = 1/5$, l_z will be given by $L_z/5$. Recall also that as we slide ϕ from 0 to π , the bulk gap of the 3D Weyl-CDW system never closes, hence the v_z is unchanged during the process. Putting this all together, we see that Eq. (43) implies that there is a $\pi \bmod 2\pi$ change in the axion angle between $\phi = 0$ and $\phi = \pi$. To be more specific, in our current examples we have $G_{xy}(\phi = 0) = -5e^2/h$ and $G_{xy}(\phi = \pi) = -4e^2/h$. This quantized change of G_{xy} or θ can be explained again using the 4D low-energy theory, as we now show.

Going back to the 4D low-energy theory, Eq. (56) predicts that if we shift k_w to $k_w + \Delta k_w$, the corresponding CI layers described by the Hamiltonian in Eq. (59)—which are localized around $z = -k_w/(2\pi q)$ —will be shifted in the z direction by $\Delta z = -\Delta k_w/(2\pi q)$. Connecting this observation back to the physical 3D Weyl-CDW system, it implies that as we slide ϕ from 0 to π , all the CI layers will be shifted by $\Delta z = -\pi/(2\pi q) = -1/(2q)$; for our choice of $q = 1/5$, this gives a shift of $\Delta z = -2.5$. We demonstrate this numerically in Figs. 4(d) and 4(e) which show the probability distribution of the eight QAH zero modes and the corresponding four nontrivial CI layers (with Chern number $C = -1$) for $\phi = \pi$. The physical interpretation of Eq. (43) is now clear: As we slide ϕ from 0 to π , the nontrivial CI layers will be shifted by $\Delta z = -2.5$ unit cells, all in the same direction. Therefore, the bottom nontrivial CI layer at $\phi = 0$ and $z = -10$ depicted in Fig. 4(c) will be shifted outside the finite sample and hence will not appear when $\phi = \pi$. At $\phi = \pi$, there will be only four nontrivial CI layers remaining. This leads to a change in the Hall conductance by e^2/h , as indicated by Eq. (43). Simultaneously, the number of QAH zero modes in the y rod decreases by 2 when we slide ϕ from 0 to π . Physically, these two QAH zero modes are pushed toward the boundary of the system, due to the shifting of the bottom nontrivial

CI layer. Therefore, their energies will be pushed toward the bulk continuum, leading to the inevitable appearance of gap-crossing bands as shown in Fig. 4(a). Numerically, we have observed that in all of our examples (Figs. 4 and 5), the zero modes in the band structure of the y rod only appear at $k_y = 0$. Therefore, as far as the zero modes are concerned, we can focus on the energy spectrum of the y rod at $k_y = 0$, as in Figs. 4(a) and 5(a). Analytically, this can be understood from the Hamiltonian of the low-energy CI Eq. (59) for each n and k_w , which has zero-energy edge modes only at $k_y = 0$ [69,91,118,120].

To summarize, we have shown that the identity Eq. (43) can be regarded as a consequence of the U(1) Landau quantization of a 4D nodal line system in which the localization centers along z of the states are directly related to k_w . We then identified k_w with the sliding phase ϕ through our dimensional promotion formalism in Sec. III. The change in conductance as a function of ϕ can thus be regarded as a physical manifestation of the *Chern number polarization*, which can alternatively be computed in terms of z -localized hybrid Wannier centers [53,106–108,121].

Having demonstrated the utility of our dimensional promotion formalism for a 3D Weyl-CDW system coupled to a commensurate CDW with $q = 1/5$, we next explore the case of incommensurate modulations which are prevalent in nature [54]. In particular, the experimentally intriguing Weyl-CDW (TaSe₄)₂I is incommensurate [36,122–125]. We still consider $H_0 + H_{\text{CDW}}(\phi)$ with $t_x = -t_y = t_z = 1$, $m = 2$, $2|\Delta| = 2$. However, we now choose the modulation $q = \tau/4$ where $\tau = (1 + \sqrt{5})/2$ is the golden ratio. For an xy slab, we choose $L_z = 21$ and for the y rod we choose $L_x \times L_z = 21 \times 21$. Since $q = \tau/4$ is an irrational number, the modulation $H_{\text{CDW}}(\phi)$ is incommensurate with H_0 . Crucially though, we can use our dimensional promotion procedure regardless of whether or not the modulation is commensurate with the underlying lattice. The U(1) gauge field to which the 4D nodal line system is coupled still takes the form in Eq. (49). The main difference is that now, the 4D system has an irrational flux $2\pi q = \pi\tau/2$ per plaquette in the zw plane. We have verified that for the xy slab we have $G_{xy}(\phi = 0) = -9e^2/h$

and $G_{xy}(\phi = \pi) = -8e^2/h$, consistent with Eq. (61). We also show in Fig. 5(a) the ϕ -sliding spectrum of the y rod at $k_y = 0$. We see that there are two fewer QAH zero modes at $\phi = \pi$ than at $\phi = 0$. The 18 and 16 QAH zero modes for $\phi = 0$ and $\phi = \pi$ are shown in Figs. 5(c) and 5(e), respectively. We again identify nine and eight nontrivial states in the xy slab at $\vec{k} = \Gamma$ for $\phi = 0$ and $\phi = \pi$, and show their probability distributions in Figs. 5(b) and 5(d), respectively. In the SM [58], we present the details of the numerical methods for identifying nontrivial states in the xy slab. The existence of nonzero QAH response and QAH zero modes can again be attributed to 4D U(1) Landau quantization which gaps the 4D nodal line system, yielding a topologically nontrivial insulating ground state. In particular, we also have $|G_{xy}(\phi = \pi) - G_{xy}(\phi = 0)| = e^2/h \bmod 2e^2/h$. This can again be understood from the shifting of nontrivial CI layers. In this case, as ϕ slides from 0 to π , all the nontrivial CI layers will be shifted downward by $\Delta z = -\pi/(2\pi q) = -2/\tau \approx -1.236$ lattice constants. The nontrivial CI layer at the bottom ($z = -10$) of Fig. 5(b) will be shifted outside the finite size system and thus the absolute value of slab Hall conductance will be changed by -1 . Consequently, the number of QAH zero modes in the y rod at $k_y = 0$ will be decreased by 2. Therefore, together with the examples in Secs. IV and V, we see that our dimensional promotion procedure provides a way to understand topological properties of systems with incommensurate modulations.

C. Weyl-CDW and 4D Chern number

We can also understand the topological properties of the Weyl-CDW model from the perspective of 4D response theory. Combining the field strength in Eq. (50) with our analysis of the Hall conductance above allows us to formulate a $(4+1)$ D field-theoretical description of the QAH response in a 3D Weyl-CDW system. The corresponding action is that of the $(4+1)$ D Chern-Simon theory [95,110],

$$S = \frac{C_2}{24\pi^2} \sum_{\mu\nu\lambda\rho\sigma} \int d^5x \epsilon^{\mu\nu\lambda\rho\sigma} A_\mu \partial_\nu A_\lambda \partial_\rho A_\sigma, \quad (62)$$

where C_2 is the second Chern number, A_μ is the electromagnetic gauge potential, and $\epsilon^{\mu\nu\lambda\rho\sigma}$ is the Levi-Civita symbol in $(4+1)$ D. The Greek indices here are taken to run over all $4+1$ dimensions. Equation (62) gives the electromagnetic response through

$$J^\mu = \frac{\delta S}{\delta A_\mu} = \frac{C_2}{32\pi^2} \sum_{\nu\lambda\rho\sigma} \epsilon^{\mu\nu\lambda\rho\sigma} F_{\nu\lambda} F_{\rho\sigma}, \quad (63)$$

where J^μ is the current density along the μ direction. Since we have $F_{zw} = 2\pi q$, an electric field E^y along y (implying $F_{1y} = E_y$) will induce a Hall current density along x through

$$J^x = q \frac{C_2}{2\pi} E^y. \quad (64)$$

Integrating this along the z direction, we find then that, with nonzero C_2 , the Hall conductance G_{xy} is proportional to qL_z . This is consistent with Eq. (61) and the recent calculation [53] showing that the Hall conductance G_{xy} of a 3D Weyl-CDW system is given by

$$G_{xy} = (|\vec{Q}|L_z + 2\theta) \cdot e^2/(2\pi h), \quad (65)$$

where L_z is the thickness of the xy slab, \vec{Q} is the CDW wave vector along z , which in our specific model system is $\vec{Q} = 2\pi q\hat{z}$, and θ is the bulk axion angle computed from the inversion-symmetric unit cell. As we take the thermodynamic limit $L_z \rightarrow \infty$, the axion angle contribution to G_{xy} becomes negligible and thus G_{xy} can also be regarded as proportional to the magnitude of CDW wave vector, which is consistent with Eq. (64). Therefore, the field strength in Eq. (50) indeed allows a sensible construction of higher dimensional continuum theory.

To see concretely that the 3D Weyl-CDW system indeed emulates a 4D system with nonzero C_2 , we notice that for both examples in Figs. 4 and 5, the system can be deformed into a limit where we have layers of decoupled CIs localized along z . In the decoupled-layer limit, for the commensurate case, for example, $q = 1/5$, where we consider the single nontrivial band in each unit cell, this implies that C_2 , which is defined through [42,71,110,121,126]

$$C_2 = \frac{1}{4\pi^2} \int_{\mathbb{T}^4} d^4k (\Omega_{xy}\Omega_{zw} + \Omega_{wx}\Omega_{zy} + \Omega_{zx}\Omega_{yw}) \quad (66)$$

becomes

$$C_2 = \frac{1}{4\pi^2} \left(\int_{\mathbb{T}^2} dk_x dk_y \Omega_{xy} \right) \left(\int_{\mathbb{T}^2} dk_z dk_w \Omega_{zw} \right) \quad (67)$$

in this limit, where $\Omega_{\mu\nu}$ is the Abelian Berry curvature in the k_μ - k_ν plane. For both examples in Figs. 4 and 5, we have identified the weak Chern number $\nu_z = -1$, implying that both systems have $\frac{1}{2\pi} \int_{\mathbb{T}^2} dk_x dk_y \Omega_{xy} = -1$. In fact, for a 3D Weyl-CDW system, it has been shown that there will always be a background QAH response in the xy plane [53], implying that in the limit of decoupled CIs, we have $\frac{1}{2\pi} \int_{\mathbb{T}^2} dk_x dk_y \Omega_{xy} \neq 0$. Furthermore, as we shift the CDW sliding phase ϕ , which is equivalent to shifting the momentum k_w , by 2π , all the Chern insulating layers will be shifted by $\Delta z = -\Delta k_w/(2\pi q) = -2\pi/(2\pi q) = -1/q$, implying a nontrivial Thouless charge pump along z . Specifically, for Fig. 4 with $q = 1/5$, all the Chern insulating layers will be shifted by $\Delta z = -5$, which is equal to the unit cell length along z , implying $|\frac{1}{2\pi} \int_{\mathbb{T}^2} dk_z dk_w \Omega_{zw}| = 1$. The fact that the 3D Weyl-CDW system can be viewed as layers of CIs [53] and the expression $\Delta z = -1/q$ governing the charge pumping along z as we vary k_w by 2π collectively predict a nonzero $\frac{1}{2\pi} \int_{\mathbb{T}^2} dk_z dk_w \Omega_{zw}$. Therefore, for a 3D Weyl-CDW system with QAH surface states [53], the corresponding 4D theory is described by a $(4+1)$ D Chern-Simon theory in Eq. (62) with nonzero C_2 . Furthermore, this result holds even as we deform away from the decoupled-layer limit, provided no energy gaps close. Thus the 3D Weyl-CDW system serves as a platform to study higher-dimensional topological field theories.

Let us conclude with two remarks. First, from the above analysis, we see that a 3D Weyl-CDW system with QAH surface states provides a platform to examine a 4D nodal line system gapped by a U(1) gauge field and carries nonzero second Chern number C_2 . Second, as opposed to Secs. IV and V where we have in higher dimensions a gapped topological phase coupled to U(1) or SU(2) gauge fields, in the 4D model promoted from a 3D Weyl-CDW system, it is precisely the coupling to a U(1) gauge field that opens up a bulk

gap, inducing emergent CI layers, QAH surface states, and nonzero C_2 .

VII. OUTLOOK

To conclude, we have shown in Secs. IV and V that higher-order topology in 3D can be probed in 2D DW systems. Furthermore, we showed in Sec. VI how 3D Weyl-CDW systems with background QAH response can be used to study 4D topology. The next and natural step is to identify 3D systems with modulations coexisting with hinge or corner modes. This will be a platform for studying four- or even higher dimensional higher-order topology. Our dimensional promotion procedure in Sec. III can also be used together with the topological classification based on crystalline symmetries [14,15,17,127] in the promoted dimensions to explore topological crystalline phases in higher dimensions. With suitably chosen modulated systems, we may either study (1) how topological crystalline insulators diagnosed by symmetry-based indicators [14,20,24,27,82,128] in the promoted dimensions respond to a background U(1) or SU(2) gauge fields or (2) how topological semimetals [129] in the promoted dimensions can be gapped by background U(1) or SU(2) gauge fields. With the dimensional promotion procedure, we may also extend our studies of topological materials to those with space groups beyond 3D, known as superspace groups [130–134]. To extract the full information in higher dimensions, a way to control the phase offset $\{\phi^{(i)}\}$ experimentally is needed, and currently applying electromagnetic fields to depin the (charge- or spin-) DWs is one practical approach [35,54]. In addition, since we can systematically compute the background continuous gauge field coupled to the dimensionally promoted model, we can again use low-dimensional modulated systems to study the low-energy dynamics in higher dimensions by minimally coupling the low-energy theory to the known continuous gauge fields as in Sec. VI. As our dimensional promotion procedure can be carried out for both commensurate and incommensurate modulations, this approach can be used to study topological properties of system with quasiperiodic potentials [46,47,70,71,121] where conventional band theory is not applicable. The general procedure will be to promote the dimension of these quasiperiodic systems and examine the response of possible topological phase in higher dimensions to a gauge field producing an irrational flux per plaquette. These techniques can be applied to analyze the DW phases in material systems of interest such as $(\text{TaSe}_4)_2\text{I}$ [35,36,124,125]

and ZrTe_5 [37–40]. This can also lead to interesting studies on the higher-dimensional Hofstadter butterfly, complementing the recent studies of Refs. [135,136]. Another interesting direction is to introduce dynamics to the DW modulation. This can happen, for example, when the phase offsets $\{\phi^{(i)}\}$ acquire nonadiabatic time dependence and become $\{\phi^{(i)}(t)\}$. Previous studies have focused on promoting the dimension of a periodically driven system to a Floquet lattice, which under certain conditions can lead to a topologically protected quantized energy pump [72,73,137]. We expect that richer phenomena in higher-dimensional space can be investigated when the DW modulations are not only periodic in real space but also (1) periodic in time or (2) have general time dependence. Finally, we have shown in Sec. V the simplest case of how SU(2) gauge field physics may be studied through a 2D modulated system. Recently, the spin-orbit-coupled Hofstadter models induced by non-Abelian SU(2) gauge fields have also been studied both in 2D [138] and 3D [139], where Dirac points with up to 16-fold degeneracy and various topological insulating states were found. We expect that 3D DW materials with different types of spin-orbit coupled modulations may enable simulation of various aspects of the physics of SU(2) gauge fields in 4D or higher dimensions, including topological states and SU(2) Hofstadter butterflies [93,138,139]. We hope that this work will lay the groundwork for the exciting future investigations mentioned above, and extend the search for exotic topological phases beyond 3D. In particular, there are many possible defects that one can imagine in a spin-orbit coupled DW order parameter, each of which may correspond to a nontrivial response to SU(2) gauge field defects in the higher-dimensional system.

ACKNOWLEDGMENTS

The authors would like to thank Y. Li and B. Wieder for fruitful discussions. This work was supported by the Alfred P. Sloan Foundation, and by the National Science Foundation under Grant No. DMR-1945058. Numerical computations made use of the Illinois Campus Cluster, a computing resource that is operated by the Illinois Campus Cluster Program (ICCP) in conjunction with the National Center for Supercomputing Applications (NCSA) and which is supported by funds from the University of Illinois at Urbana-Champaign. Numerical calculations in this work employed the open-source PYTHTB package [140].

[1] L. Fu, *Phys. Rev. Lett.* **106**, 106802 (2011).
 [2] T. H. Hsieh, H. Lin, J. Liu, W. Duan, A. Bansil, and L. Fu, *Nat. Commun.* **3**, 982 (2012).
 [3] Y. Ando and L. Fu, *Annu. Rev. Condens. Matter Phys.* **6**, 361 (2015).
 [4] T. L. Hughes, E. Prodan, and B. A. Bernevig, *Phys. Rev. B* **83**, 245132 (2011).
 [5] A. M. Turner, Y. Zhang, and A. Vishwanath, *Phys. Rev. B* **82**, 241102(R) (2010).

[6] A. M. Turner, Y. Zhang, R. S. K. Mong, and A. Vishwanath, *Phys. Rev. B* **85**, 165120 (2012).
 [7] C. L. Kane and E. J. Mele, *Phys. Rev. Lett.* **95**, 226801 (2005).
 [8] B. A. Bernevig, T. L. Hughes, and S.-C. Zhang, *Science* **314**, 1757 (2006).
 [9] M. König, S. Wiedmann, C. Brüne, A. Roth, H. Buhmann, L. W. Molenkamp, X.-L. Qi, and S.-C. Zhang, *Science* **318**, 766 (2007).

- [10] L. Fu, C. L. Kane, and E. J. Mele, *Phys. Rev. Lett.* **98**, 106803 (2007).
- [11] Y. Xia, D. Qian, D. Hsieh, L. Wray, A. Pal, H. Lin, A. Bansil, D. Grauer, Y. S. Hor, R. J. Cava, and M. Z. Hasan, *Nat. Phys.* **5**, 398 (2009).
- [12] Z. Wang, A. Alexandradinata, R. J. Cava, and B. A. Bernevig, *Nature (London)* **532**, 189 (2016).
- [13] F. Schindler, A. M. Cook, M. G. Vergniory, Z. Wang, S. S. P. Parkin, B. A. Bernevig, and T. Neupert, *Sci. Adv.* **4**, eaat0346 (2018).
- [14] H. C. Po, A. Vishwanath, and H. Watanabe, *Nat. Commun.* **8**, 50 (2017).
- [15] E. Khalaf, *Phys. Rev. B* **97**, 205136 (2018).
- [16] W. A. Benalcazar, B. A. Bernevig, and T. L. Hughes, *Science* **357**, 61 (2017).
- [17] B. Bradlyn, L. Elcoro, J. Cano, M. G. Vergniory, Z. Wang, C. Felser, M. I. Aroyo, and B. A. Bernevig, *Nature (London)* **547**, 298 (2017).
- [18] M. Vergniory, L. Elcoro, C. Felser, B. Bernevig, and Z. Wang, *Nature (London)* **566**, 480 (2019).
- [19] T. Zhang, Y. Jiang, Z. Song, H. Huang, Y. He, Z. Fang, H. Weng, and C. Fang, *Nature (London)* **566**, 475 (2019).
- [20] F. Tang, H. C. Po, A. Vishwanath, and X. Wan, *Nat. Phys.* **15**, 470 (2019).
- [21] Y. Xu, L. Elcoro, Z.-D. Song, B. J. Wieder, M. Vergniory, N. Regnault, Y. Chen, C. Felser, and B. A. Bernevig, *Nature (London)* **586**, 702 (2020).
- [22] J. Kruthoff, J. de Boer, J. van Wezel, C. L. Kane, and R.-J. Slager, *Phys. Rev. X* **7**, 041069 (2017).
- [23] L. Fu and C. L. Kane, *Phys. Rev. B* **76**, 045302 (2007).
- [24] H. C. Po, *J. Phys.: Condens. Matter* **32**, 263001 (2020).
- [25] J. Cano and B. Bradlyn, *Ann. Rev. Condens. Matter Phys.* **12**, 225 (2020).
- [26] L. Elcoro, B. J. Wieder, Z. Song, Y. Xu, B. Bradlyn, and B. A. Bernevig, [arXiv:2010.00598](https://arxiv.org/abs/2010.00598).
- [27] H. Watanabe, H. C. Po, and A. Vishwanath, *Sci. Adv.* **4**, eaat8685 (2018).
- [28] R.-X. Zhang and C.-X. Liu, *Phys. Rev. B* **91**, 115317 (2015).
- [29] A. Bouhon, G. F. Lange, and R.-J. Slager, [arXiv:2010.10536](https://arxiv.org/abs/2010.10536).
- [30] Z. Wang and S.-C. Zhang, *Phys. Rev. B* **87**, 161107(R) (2013).
- [31] Y. You, G. Y. Cho, and T. L. Hughes, *Phys. Rev. B* **94**, 085102 (2016).
- [32] A. A. Zyuzin and A. A. Burkov, *Phys. Rev. B* **86**, 115133 (2012).
- [33] A. A. Zyuzin, S. Wu, and A. A. Burkov, *Phys. Rev. B* **85**, 165110 (2012).
- [34] J. Maciejko and R. Nandkishore, *Phys. Rev. B* **90**, 035126 (2014).
- [35] J. Gooth, B. Bradlyn, S. Honnali, C. Schindler, N. Kumar, J. Noky, Y. Qi, C. Shekhar, Y. Sun, Z. Wang, B. A. Bernevig, and C. Felser, *Nature (London)* **575**, 315 (2019).
- [36] W. Shi, B. J. Wieder, H. L. Meyerheim, Y. Sun, Y. Zhang, Y. Li, L. Shen, Y. Qi, L. Yang, J. Jena, P. Werner, K. Koepf, S. Parkin, Y. Chen, C. Felser, B. A. Bernevig, and Z. Wang, *Nat. Phys.* **17**, 381 (2021).
- [37] F. Tang, Y. Ren, P. Wang, R. Zhong, J. Schneeloch, S. A. Yang, K. Yang, P. A. Lee, G. Gu, Z. Qiao *et al.*, *Nature (London)* **569**, 537 (2019).
- [38] F. Qin, S. Li, Z. Z. Du, C. M. Wang, W. Zhang, D. Yu, H.-Z. Lu, and X. C. Xie, *Phys. Rev. Lett.* **125**, 206601 (2020).
- [39] Z. Song, Z. Fang, and X. Dai, *Phys. Rev. B* **96**, 235104 (2017).
- [40] X.-T. Zhang and R. Shindou, *Phys. Rev. B* **95**, 205108 (2017).
- [41] T. Ozawa, H. M. Price, A. Amo, N. Goldman, M. Hafezi, L. Lu, M. C. Rechtsman, D. Schuster, J. Simon, O. Zilberberg, and I. Carusotto, *Rev. Mod. Phys.* **91**, 015006 (2019).
- [42] T. Ozawa, H. M. Price, N. Goldman, O. Zilberberg, and I. Carusotto, *Phys. Rev. A* **93**, 043827 (2016).
- [43] I. H. Grinberg, M. Lin, C. Harris, W. A. Benalcazar, C. W. Peterson, T. L. Hughes, and G. Bahl, *Nat. Commun.* **11**, 974 (2020).
- [44] F. A. An, E. J. Meier, and B. Gadway, *Sci. Adv.* **3**, e1602685 (2017).
- [45] D. R. Hofstadter, *Phys. Rev. B* **14**, 2239 (1976).
- [46] Y. E. Kraus and O. Zilberberg, *Phys. Rev. Lett.* **109**, 116404 (2012).
- [47] Y. E. Kraus, Y. Lahini, Z. Ringel, M. Verbin, and O. Zilberberg, *Phys. Rev. Lett.* **109**, 106402 (2012).
- [48] D. J. Thouless, *Phys. Rev. B* **27**, 6083 (1983).
- [49] Q. Niu and D. Thouless, *J. Phys. A: Math. Gen.* **17**, 2453 (1984).
- [50] P. Marra and M. Nitta, *Phys. Rev. Research* **2**, 042035(R) (2020).
- [51] Q.-B. Zeng, Y.-B. Yang, and Y. Xu, *Phys. Rev. B* **101**, 241104(R) (2020).
- [52] M. J. Rice and E. J. Mele, *Phys. Rev. Lett.* **49**, 1455 (1982).
- [53] B. J. Wieder, K.-S. Lin, and B. Bradlyn, *Phys. Rev. Research* **2**, 042010(R) (2020).
- [54] G. Grüner, *Rev. Mod. Phys.* **60**, 1129 (1988).
- [55] C.-H. Hsu, X. Zhou, T.-R. Chang, Q. Ma, N. Gedik, A. Bansil, S.-Y. Xu, H. Lin, and L. Fu, *Proc. Natl. Acad. Sci.* **116**, 13255 (2019).
- [56] A. K. Nayak, J. Reiner, R. Queiroz, H. Fu, C. Shekhar, B. Yan, C. Felser, N. Avraham, and H. Beidenkopf, *Sci. Adv.* **5**, eaax6996 (2019).
- [57] F. Schindler, Z. Wang, M. G. Vergniory, A. M. Cook, A. Murani, S. Sengupta, A. Y. Kasumov, R. Deblock, S. Jeon, I. Drozdov *et al.*, *Nat. Phys.* **14**, 918 (2018).
- [58] See Supplemental Material at <http://link.aps.org/supplemental/10.1103/PhysRevB.103.245107> for a description of the general dimensional promotion method, additional examples of dimensional promotion, and other numerical calculations, which includes Refs. [59,135,141–144].
- [59] W. P. Su, J. R. Schrieffer, and A. J. Heeger, *Phys. Rev. Lett.* **42**, 1698 (1979).
- [60] W. Kohn, *Phys. Rev.* **115**, 809 (1959).
- [61] C. Brouder, G. Panati, M. Calandra, C. Mourougane, and N. Marzari, *Phys. Rev. Lett.* **98**, 046402 (2007).
- [62] N. Marzari, A. A. Mostofi, J. R. Yates, I. Souza, and D. Vanderbilt, *Rev. Mod. Phys.* **84**, 1419 (2012).
- [63] W. Shockley, *Phys. Rev.* **56**, 317 (1939).
- [64] D. Xiao, M.-C. Chang, and Q. Niu, *Rev. Mod. Phys.* **82**, 1959 (2010).
- [65] A. Alexandradinata, X. Dai, and B. A. Bernevig, *Phys. Rev. B* **89**, 155114 (2014).
- [66] R. D. King-Smith and D. Vanderbilt, *Phys. Rev. B* **47**, 1651(R) (1993).
- [67] D. J. Thouless, M. Kohmoto, M. P. Nightingale, and M. den Nijs, *Phys. Rev. Lett.* **49**, 405 (1982).

- [68] Q. Niu, D. J. Thouless, and Y.-S. Wu, *Phys. Rev. B* **31**, 3372 (1985).
- [69] B. A. Bernevig and T. L. Hughes, *Topological Insulators and Topological Superconductors* (Princeton University Press, Princeton, NJ, 2013).
- [70] T. Rasing, *Phys. Rev. Lett.* **53**, 388 (1984).
- [71] Y. E. Kraus, Z. Ringel, and O. Zeitler, *Phys. Rev. Lett.* **111**, 226401 (2013).
- [72] I. Martin, G. Refael, and B. Halperin, *Phys. Rev. X* **7**, 041008 (2017).
- [73] Y. Peng and G. Refael, *Phys. Rev. B* **97**, 134303 (2018).
- [74] Throughout this paper, we will use square brackets to denote matrices and matrix-valued functions.
- [75] R. Peierls, *Z. Phys.* **80**, 763 (1933).
- [76] J. Zak, *Phys. Rev. Lett.* **62**, 2747 (1989).
- [77] I. Petrides and O. Zeitler, *Phys. Rev. Research* **2**, 022049(R) (2020).
- [78] S. Ryu, A. P. Schnyder, A. Furusaki, and A. W. Ludwig, *New J. Phys.* **12**, 065010 (2010).
- [79] A. Kitaev, *AIP Conf. Proc.* **1134**, 22 (2009).
- [80] F. D. M. Haldane, *Phys. Rev. Lett.* **61**, 2015 (1988).
- [81] B. J. Wieder and B. A. Bernevig, [arXiv:1810.02373](https://arxiv.org/abs/1810.02373).
- [82] E. Khalaf, H. C. Po, A. Vishwanath, and H. Watanabe, *Phys. Rev. X* **8**, 031070 (2018).
- [83] Z. Song, T. Zhang, Z. Fang, and C. Fang, *Nat. Commun.* **9**, 3530 (2018).
- [84] Z. Wang, B. J. Wieder, J. Li, B. Yan, and B. A. Bernevig, *Phys. Rev. Lett.* **123**, 186401 (2019).
- [85] J. Yu, Z.-D. Song, and C.-X. Liu, *Phys. Rev. Lett.* **125**, 036401 (2020).
- [86] H. Kim, K. Shiozaki, and S. Murakami, *Phys. Rev. B* **100**, 165202 (2019).
- [87] R. Takahashi, Y. Tanaka, and S. Murakami, *Phys. Rev. Research* **2**, 013300 (2020).
- [88] O. Pozo, C. Repellin, and A. G. Grushin, *Phys. Rev. Lett.* **123**, 247401 (2019).
- [89] W. A. Benalcazar, T. Li, and T. L. Hughes, *Phys. Rev. B* **99**, 245151 (2019).
- [90] B. J. Wieder, Z. Wang, J. Cano, X. Dai, L. M. Schoop, B. Bradlyn, and B. A. Bernevig, *Nat. Commun.* **11**, 627 (2020).
- [91] M. Z. Hasan and C. L. Kane, *Rev. Mod. Phys.* **82**, 3045 (2010).
- [92] N. Varnava and D. Vanderbilt, *Phys. Rev. B* **98**, 245117 (2018).
- [93] Y. Li, *Phys. Rev. B* **91**, 195133 (2015).
- [94] Y. Li, S.-C. Zhang, and C. Wu, *Phys. Rev. Lett.* **111**, 186803 (2013).
- [95] S.-C. Zhang and J. Hu, *Science* **294**, 823 (2001).
- [96] N. Goldman, I. Satija, P. Nikolic, A. Bermudez, M. A. Martin-Delgado, M. Lewenstein, and I. B. Spielman, *Phys. Rev. Lett.* **105**, 255302 (2010).
- [97] X.-L. Qi and S.-C. Zhang, *Phys. Rev. Lett.* **101**, 086802 (2008).
- [98] F. Mei, S.-L. Zhu, Z.-M. Zhang, C. H. Oh, and N. Goldman, *Phys. Rev. A* **85**, 013638 (2012).
- [99] B. Estienne, S. M. Haaker, and K. Schoutens, *New J. Phys.* **13**, 045012 (2011).
- [100] T. Eguchi, P. B. Gilkey, and A. J. Hanson, *Phys. Rep.* **66**, 213 (1980).
- [101] L. Fu and C. L. Kane, *Phys. Rev. B* **74**, 195312 (2006).
- [102] J. C. Y. Teo and C. L. Kane, *Phys. Rev. B* **82**, 115120 (2010).
- [103] D. Sehayek, M. Thakurathi, and A. A. Burkov, *Phys. Rev. B* **102**, 115159 (2020).
- [104] I. A. Cohn, S. G. Zvybtsev, A. P. Orlov, and S. V. Zaitsev-Zotov, *JETP Lett.* **112**, 88 (2020).
- [105] E. Bobrow, C. Sun, and Y. Li, *Phys. Rev. Research* **2**, 012078(R) (2020).
- [106] J. Yu, B. J. Wieder, and C.-X. Liu, [arXiv:2008.10620](https://arxiv.org/abs/2008.10620).
- [107] T. Olsen, T. Rauch, D. Vanderbilt, and I. Souza, *Phys. Rev. B* **102**, 035166 (2020).
- [108] N. Varnava, I. Souza, and D. Vanderbilt, *Phys. Rev. B* **101**, 155130 (2020).
- [109] T. M. McCormick, I. Kimchi, and N. Trivedi, *Phys. Rev. B* **95**, 075133 (2017).
- [110] X.-L. Qi, T. L. Hughes, and S.-C. Zhang, *Phys. Rev. B* **78**, 195424 (2008).
- [111] M. Kohmoto, B. I. Halperin, and Y.-S. Wu, *Phys. Rev. B* **45**, 13488 (1992).
- [112] B. I. Halperin, *Jpn. J. Appl. Phys.* **26**, 1913 (1987).
- [113] R. Winkler and U. Rössler, *Phys. Rev. B* **48**, 8918 (1993).
- [114] R. Winkler and U. Rössler, *Surf. Sci.* **305**, 295 (1994).
- [115] J. Linder, T. Yokoyama, and A. Sudbø, *Phys. Rev. B* **80**, 205401 (2009).
- [116] M. König, H. Buhmann, L. W. Molenkamp, T. Hughes, C.-X. Liu, X.-L. Qi, and S.-C. Zhang, *J. Phys. Soc. Jpn.* **77**, 031007 (2008).
- [117] B. Zhou, H.-Z. Lu, R.-L. Chu, S.-Q. Shen, and Q. Niu, *Phys. Rev. Lett.* **101**, 246807 (2008).
- [118] X.-L. Qi and S.-C. Zhang, *Rev. Mod. Phys.* **83**, 1057 (2011).
- [119] C. Li, C. M. Wang, B. Wan, X. Wan, H.-Z. Lu, and X. C. Xie, *Phys. Rev. Lett.* **120**, 146602 (2018).
- [120] R. Jackiw and C. Rebbi, *Phys. Rev. D* **13**, 3398 (1976).
- [121] O. Zeitler, S. Huang, J. Guglielmon, M. Wang, K. P. Chen, Y. E. Kraus, and M. C. Rechtsman, *Nature (London)* **553**, 59 (2018).
- [122] Z. Z. Wang, M. Saint-Lager, P. Monceau, M. Renard, P. Gressier, A. Meerschaut, L. Guemas, and J. Rouxel, *Solid State Commun.* **46**, 325 (1983).
- [123] K.-B. Lee, D. Davidov, and A. Heeger, *Solid State Commun.* **54**, 673 (1985).
- [124] C. Tournier-Colletta, L. Moreschini, G. Autes, S. Moser, A. Crepaldi, H. Berger, A. L. Walter, K. S. Kim, A. Bostwick, P. Monceau, E. Rotenberg, O. V. Yazyev, and M. Grioni, *Phys. Rev. Lett.* **110**, 236401 (2013).
- [125] Y. Zhang, L.-F. Lin, A. Moreo, S. Dong, and E. Dagotto, *Phys. Rev. B* **101**, 174106 (2020).
- [126] H. M. Price, O. Zeitler, T. Ozawa, I. Carusotto, and N. Goldman, *Phys. Rev. Lett.* **115**, 195303 (2015).
- [127] C.-K. Chiu, J. C. Y. Teo, A. P. Schnyder, and S. Ryu, *Rev. Mod. Phys.* **88**, 035005 (2016).
- [128] H. C. Po, H. Watanabe, and A. Vishwanath, *Phys. Rev. Lett.* **121**, 126402 (2018).
- [129] N. P. Armitage, E. J. Mele, and A. Vishwanath, *Rev. Mod. Phys.* **90**, 015001 (2018).
- [130] L. Elcoro and J. M. Perez-Mato, *Phys. Rev. B* **54**, 12115 (1996).

- [131] A. Janner and T. Janssen, *Physica A* **99**, 47 (1979).
- [132] T. Janssen and A. Janner, *Acta Crystallogr. Sect. B* **70**, 617 (2014).
- [133] P. Bak and T. Janssen, *Phys. Rev. B* **17**, 436 (1978).
- [134] P. M. de Wolff, T. Janssen, and A. Janner, *Acta Crystallogr. Sect. A* **37**, 625 (1981).
- [135] B. Lian, F. Xie, and B. A. Bernevig, *Phys. Rev. B* **102**, 041402(R) (2020).
- [136] J. Herzog-Arbeitman, Z.-D. Song, N. Regnault, and B. A. Bernevig, *Phys. Rev. Lett.* **125**, 236804 (2020).
- [137] F. Nathan, I. Martin, and G. Refael, *Phys. Rev. B* **99**, 094311 (2019).
- [138] Y. Yang, B. Zhen, J. D. Joannopoulos, and M. Soljačić, *Light: Sci. Appl.* **9**, 177 (2020).
- [139] V. Liu, Y. Yang, J. D. Joannopoulos, and M. Soljačić, [arXiv:2010.11308](https://arxiv.org/abs/2010.11308).
- [140] S. Coh and D. Vanderbilt, Python Tight Binding (PythTB), <http://www.physics.rutgers.edu/pythtb> (2013).
- [141] R. Resta, *Rev. Mod. Phys.* **66**, 899 (1994).
- [142] L. Fidkowski, T. S. Jackson, and I. Klich, *Phys. Rev. Lett.* **107**, 036601 (2011).
- [143] R. Yu, X. L. Qi, A. Bernevig, Z. Fang, and X. Dai, *Phys. Rev. B* **84**, 075119 (2011).
- [144] A. Alexandradinata and B. A. Bernevig, *Phys. Rev. B* **93**, 205104 (2016).